

EFFICIENT KRYLOV METHODS FOR LINEAR RESPONSE IN PLANE-WAVE ELECTRONIC STRUCTURE CALCULATIONS*

MICHAEL F. HERBST[†] AND BONAN SUN^{†‡}

Abstract. We propose a novel algorithm based on inexact GMRES methods for linear response calculations in density functional theory. Such calculations require iteratively solving a nested linear problem $\mathcal{E}\delta\rho = b$ to obtain the variation of the electron density $\delta\rho$. Notably each application of the dielectric operator \mathcal{E} in turn requires the iterative solution of multiple linear systems, the Sternheimer equations. We develop computable bounds to estimate the accuracy of the density variation given the tolerances to which the Sternheimer equations have been solved. Based on this result we suggest reliable strategies for adaptively selecting the convergence tolerances of the Sternheimer equations, such that each applications of \mathcal{E} is no more accurate than needed. Experiments on challenging materials systems of practical relevance demonstrate our strategies to achieve superlinear convergence as well as a reduction of computational time by about 40% while preserving the accuracy of the returned response solution. Our algorithm seamlessly combines with standard preconditioning approaches known from the context of self-consistent field problems making it a promising framework for efficient response solvers based on Krylov subspace techniques.

Key words. Electronic-structure theory, Linear response theory, Inexact Krylov subspace methods, Inexact GMRES, Nested linear problems, Density-functional theory, Density-functional perturbation theory

MSC codes. 65F10, 65Z05, 81V55, 81-08, 81Q15

1. Introduction. First-principle simulations of the electronic structure are a crucial ingredient to drive research in physics, chemistry, materials science and engineering. Due to their favourable balance of cost and accuracy Kohn-Sham density-functional theory (DFT) calculations are particularly popular and nowadays routinely run in the millions in scientific workflows [38, 17] to predict material properties. Notably experiments probe material properties by observing how the material changes under a variation of external conditions, such as an applied field or an imposed strain. Computationally this can be modelled as the response of a material’s ground state (GS) to a perturbation of the external potential. In this sense materials properties can be identified with derivatives of the ground state with respect to external parameters. For example interatomic forces are obtained as the derivative of the GS energy versus nuclear positions and polarisabilities as the second derivative of the energy with respect to the electric field. Other properties (such as phonon or Raman spectra) require even high-order energy derivatives [3, 48, 54]. Beyond physical observables more recent applications of DFT derivatives include (a) the design of machine-learned (ML) exchange-correlation functionals [39, 36, 18, 55] — where derivatives of the GS wrt. the ML parameters are needed — and (b) the computation of *a posteriori* error estimates [32, 19] — where derivatives wrt. the perturbation induced by considering a larger discretisation basis are required.

The application of perturbation theory to the special case of DFT — with the

*Submitted to the editors on DATE

Funding: MFH acknowledges support by the Swiss National Science Foundation (SNSF, Grant No. 221186) as well as the NCCR MARVEL, a National Centre of Competence in Research, funded by the SNSF (Grant No. 205602).

[†]Mathematics for Materials Modelling, Institute of Mathematics & Institute of Materials, École Polytechnique Fédérale de Lausanne, 1015 Lausanne, Switzerland (michael.herbst@epfl.ch, bonan.sun@epfl.ch)

[‡]Max Planck Institute for Dynamics of Complex Technical Systems, 39106 Magdeburg, Germany (bsun@mpi-magdeburg.mpg.de)

goal to compute the aforementioned GS derivatives — is known as density functional perturbation theory (DFPT) [4, 28, 24, 25]. See [45] for its applications in quantum chemistry, [3] for the application to phonons in crystal systems, and [43, 11] for recent performance improvements motivated by analytical study. See also [15] for a mathematical analysis in the context of the reduced Hartree-Fock model, a model closely related to DFT.

In particular the computation of the *linear response* $\delta\rho$ to the electronic density under a perturbation δV_0 of the external potential plays a foundational role in DFPT: due to Wigner’s $(2n + 1)$ rule computing the $2n$ -th and $(2n + 1)$ -st derivatives of the GS energy requires computing the first n derivatives of the GS density [24, 25]. Therefore efficiently solving the linear response problem is required for computing the *first and all higher order* GS energy derivatives.

Computing the linear response mapping $\delta V_0 \mapsto \delta\rho$ requires solving the Dyson equation

$$(1.1) \quad \mathcal{E}\delta\rho = \chi_0\delta V_0.$$

It involves the independent particle susceptibility χ_0 as well as the (adjoint of the) dielectric operator \mathcal{E} , which itself also depends on χ_0 . Crucially, a single application of χ_0 (thus also \mathcal{E}) requires itself solving N_{occ} linear systems, the Sternheimer equations (SE). Here N_{occ} , the number of DFT eigenstates with non-zero occupation, notably scales linearly with the number of electrons in the material.

In this work we consider in particular the setting of “large basis sets”, such as plane-wave discretisations, where both the Dyson equation as well as the SE need to be solved with iterative methods. A delicate issue for obtaining an efficient iterative solver for this nested set of problems is the selection of the convergence criteria when solving the inner SEs: due to the sheer number of solves too tight a tolerance quickly drives up computational cost, while on the other hand too loose a tolerance can lead to inaccurate responses $\delta\rho$. Moreover for some materials (such as metals) both the Dyson equation as well as the inner SEs can become poorly conditioned [11], such that (a) tight convergence tolerances may be difficult to achieve and (b) numerical noise may amplify. These aspects illustrate why efficient response calculations remain a challenge in practical electronic structure simulations [27] — in particular for metals and for disordered materials (where N_{occ} is large).

Our main contribution in this work is an algorithm for solving the Dyson equation (1.1), in which for each individual SE the convergence threshold is adaptively selected to reduce overall computational cost. This algorithm is backed up by a theoretical analysis (Theorem 3.7) demonstrating that despite using inexact solves the algorithm still obtains a solution to the Dyson equation within the prescribed accuracy. A key ingredient is a novel rigorous bound for the error in the application of the linear operator \mathcal{E} resulting from inexact SE solves (Lemma 3.5), combined with the inexact GMRES framework of Simoncini and Szyld [50]. For the latter our work also develops an extension to estimate the smallest singular value of the upper Hessenberg matrix on the fly, which is generally applicable beyond the Dyson equation context.

Beyond our guaranteed bound we further develop a series of physically motivated approximations, which enable additional savings in computational cost while hardly impacting accuracy (Section 3.3). We further analyse scaling of these strategies with increasing system size to ensure that our results do not deteriorate when targeting larger materials. In experiments on non-trivial material systems — a metallic supercell and a Heusler alloy material — our recommended **bal** (balanced) algorithm achieves

a reduction in the computational time of about 40% compared to approaches with fixed SE tolerances of similar accuracy.

Our developments complement recent techniques to improve DFPT convergence. Throughout this work we will employ the Schur complement approach suggested in [11] for the SE. On metallic systems we additionally employed the Kerker preconditioner within the inexact GMRES for solving the Dyson equations — leading to a speed-up of about a factor of 3 if all techniques are combined. Surprisingly, this use of the Kerker preconditioner when solving the Dyson equation does not seem to be established in the literature — despite Kerker being widely employed when obtaining the DFT ground state using self-consistent field techniques.

While developed for the setting of plane-wave DFT we remark that our ideas can be easily extended to related mean-field models such as Hartree-Fock [41] or the Gross-Pitaevskii equations (GPE) [2] due to the closely related mathematical structure [7]. Moreover our modifications to the inexact GMRES framework are general and could be applied to other nested linear problems.

The remainder of this paper is structured as follows. In Section 2, we review the mathematical formulation of DFT and DFPT as well as its numerical discretisation in plane-wave basis. In Section 3, we derive computable error bounds quantifying how inaccuracies in Sternheimer solutions propagate to the solution of the Dyson equation as well as practical strategies for selecting SE convergence thresholds. Numerical experiments confirming the efficiency gains of our algorithm are presented in Section 4.

2. Mathematical framework.

2.1. Kohn-Sham density functional theory for periodic systems. We consider a simulation cell $\Omega = [0, 1)\mathbf{a}_1 + [0, 1)\mathbf{a}_2 + [0, 1)\mathbf{a}_3$ for some not necessarily orthonormal basis $(\mathbf{a}_1, \mathbf{a}_2, \mathbf{a}_3) \in \mathbb{R}^3$ and denote the associated periodic lattice in position space by $\mathbb{L} = \mathbb{Z}\mathbf{a}_1 + \mathbb{Z}\mathbf{a}_2 + \mathbb{Z}\mathbf{a}_3$ as well as reciprocal lattice by

$$(2.1) \quad \mathbb{L}^* = \mathbb{Z}\mathbf{b}_1 + \mathbb{Z}\mathbf{b}_2 + \mathbb{Z}\mathbf{b}_3, \quad \text{with} \quad \mathbf{b}_i \cdot \mathbf{a}_j = 2\pi\delta_{ij}, \quad i, j = 1, 2, 3.$$

The space of locally square-integrable \mathbb{L} -periodic functions is given by

$$(2.2) \quad L^2_\Omega(\mathbb{R}^3, \mathbb{C}) = \left\{ u : \mathbb{R}^3 \rightarrow \mathbb{C} \mid u(\mathbf{r} + \mathbf{R}) = u(\mathbf{r}), \forall \mathbf{r} \in \mathbb{R}^3, \mathbf{R} \in \mathbb{L}, \int_\Omega |u(\mathbf{r})|^2 d\mathbf{r} < \infty \right\}$$

endowed with the usual inner product $\langle \cdot, \cdot \rangle$. We consider the case of a system containing an even $N \in \mathbb{N}$ number of electrons in a spin-paired state at finite smearing temperature $T > 0$, for which the DFT ground-state is defined by an L^2_Ω -orthonormal set of orbitals $(\phi_n)_{n \in \mathbb{N}}$ obtained as eigenfunctions of the Kohn-Sham Hamiltonian H_ρ

$$(2.3) \quad H_\rho \phi_n(\mathbf{r}) = \epsilon_n \phi_n(\mathbf{r}), \quad \epsilon_1 \leq \epsilon_2 \leq \dots, \quad \langle \phi_n, \phi_m \rangle = \delta_{nm}$$

where $(\epsilon_n)_{n \in \mathbb{N}}$ are the orbital energies. In atomic units the Hamiltonian reads as

$$(2.4) \quad H_\rho = -\frac{1}{2}\Delta + V_{\text{ext}}(\mathbf{r}) + V_\rho^{\text{Hxc}}(\mathbf{r}),$$

where V_{ext} is the external potential modelling the interaction of the electrons with the environment (e.g. such as the potential generated by the nuclei of the material) and $V_\rho^{\text{Hxc}}(\mathbf{r}) = V_\rho^{\text{H}}(\mathbf{r}) + V_\rho^{\text{xc}}(\mathbf{r})$ is the Hartree-exchange-correlation potential modelling the electron-electron interactions. Both V_ρ^{Hxc} and V_{ext} are \mathbb{L} -periodic functions. The

Hartree potential V_ρ^{H} is obtained as the unique zero-mean solution of the periodic Poisson equation $-\Delta V_\rho^{\text{H}}(\mathbf{r}) = 4\pi \left(\rho(\mathbf{r}) - \frac{1}{|\Omega|} \int_\Omega \rho d\mathbf{r} \right)$ and V_ρ^{xc} is the exchange-correlation potential, both depending on ρ . We remark that H_ρ is a self-adjoint operator on L_Ω^2 , which is bounded below and has compact resolvent, such that its spectrum is indeed composed of a nondecreasing sequence of eigenvalues $(\epsilon_n)_{n \in \mathbb{N}}$ accumulating at $+\infty$.

The ground-state density ρ is defined in terms of the Kohn-Sham orbitals $(\phi_n)_{n \in \mathbb{N}}$

$$(2.5) \quad \rho(\mathbf{r}) = \sum_{n=1}^{\infty} f_n |\phi_n(\mathbf{r})|^2 \quad \text{with} \quad f_n = f_{\text{FD}} \left(\frac{\epsilon_n - \epsilon_{\text{F}}}{T} \right),$$

where $f_n \in [0, 2)$ are the occupation numbers and f_{FD} is the occupation function. The Fermi level ϵ_{F} is chosen as the real number such that $\int_\Omega \rho(\mathbf{r}) d\mathbf{r} = \sum_{n=1}^{\infty} f_n = N$. For simplicity we consider the case of a monotonic smearing function, such as the Fermi-Dirac function $f_{\text{FD}}(x) = 2/(1 + e^x)$.

Since H_ρ depends on ρ , which in turn depends on the eigenfunctions ϕ_n of H_ρ , (2.3) is a non-linear eigenvalue problem, which is usually equivalently written as a fixed-point problem in the density

$$(2.6) \quad \rho = \mathcal{F}_{\text{KS}} (V_{\text{ext}} + V_\rho^{\text{Hxc}}).$$

Here we introduced the potential-to-density map

$$(2.7) \quad \mathcal{F}_{\text{KS}} : V \mapsto \rho = \sum_{n=1}^{\infty} f_{\text{FD}} \left(\frac{\epsilon_n - \epsilon_{\text{F}}}{T} \right) |\phi_n|^2.$$

with $(\phi_n)_{n \in \mathbb{N}}$ being the L_Ω^2 -orthonormal eigenfunctions of $-\frac{1}{2}\Delta + V$ ordered by non-decreasing corresponding eigenvalues $(\epsilon_n)_{n \in \mathbb{N}}$. The form (2.6) of the non-linear eigenvalue problem (2.3) is called self-consistent field (SCF) problem and is usually solved using (preconditioned, accelerated) fixed-point iterations, see [42, 12, 31, 13] for details. Notably these methods require in each step the evaluation of \mathcal{F}_{KS} on a given iterate ρ_n , which in turn implies a diagonalisation of H_{ρ_n} . For a mathematical presentation of SCF methods see [12, 41, 13] and consider [30, 31] for an in-depth discussion of the practical challenges of obtaining robust SCF algorithms.

2.2. Density functional perturbation theory (DFPT). Having solved the SCF problem (2.6) we obtain the DFT ground-state density ρ . Notably (2.6) and thus the solution ρ depends on V_{ext} , defining thus an implicit function $V_{\text{ext}} \mapsto \rho$ mapping from the external potential V_{ext} to the self-consistent density ρ . The goal of DFPT is to compute derivatives of this function, which thus allows to study how the ground state density responds to perturbations in the external conditions of the electrons (displacement of nuclei, changes to the electromagnetic field, etc.).

Let δV_0 denote an infinitesimal local perturbation of V_{ext} , i.e. a perturbation that can be written as a multiplication operator involving the periodic function $\mathbf{r} \mapsto \delta V_0(\mathbf{r})$. We now compute the linearisation of (2.6) using the chain rule leading to the Dyson equation

$$(2.8) \quad \delta \rho = \underbrace{\mathcal{F}'_{\text{KS}}(V_{\text{ext}} + V_\rho^{\text{Hxc}})}_{\chi_0} (\delta V_0 + K_\rho^{\text{Hxc}} \delta \rho) \iff (1 - \chi_0 K_\rho^{\text{Hxc}}) \delta \rho = \chi_0 \delta V_0,$$

where the independent-particle susceptibility χ_0 is the derivative of \mathcal{F}_{KS} and Hartree-exchange-correlation kernel K_ρ^{Hxc} is the derivative of $\rho \mapsto V_\rho^{\text{Hxc}}$, both evaluated at the

self-consistent potential and density, respectively. Given an infinitesimal perturbation $\delta V_0(\mathbf{r})$ the first-order approximation of the variation of the electron density $\delta\rho$ is thus obtained by solving the Dyson equation linear system (2.8). Notably the operator

$$(2.9) \quad \mathcal{E} := 1 - \chi_0 K_\rho^{\text{Hxc}}$$

turns out to be the adjoint of the dielectric operator $1 - K_\rho^{\text{Hxc}} \chi_0$ [1, 30]. Therefore we refer to \mathcal{E} as the dielectric adjoint from this point onwards.

As we will detail in Section 2.3.5, the Dyson equation (2.8) is typically solved iteratively, such that an efficient application of both K_ρ^{Hxc} and χ_0 is crucial. The kernel $K_\rho^{\text{Hxc}} = K_\rho^{\text{H}} + K_\rho^{\text{xc}}$ is the sum of two terms, the Coulomb kernel K_ρ^{H} and the exchange-correlation kernel K_ρ^{xc} . The former is diagonal in a plane-wave basis and the latter can be applied using a real-space convolution, thus both are indeed efficient to treat.

In contrast, applying the independent particle susceptibility $\chi_0 : \delta V \mapsto \delta\rho_0$ is considerably more challenging and — if done exactly — would in fact involve an infinite sum over all eigenpairs (ϵ_n, ϕ_n) of H_ρ . However, typical smearing functions (such as f_{FD}) rapidly decay to zero as $x \rightarrow \infty$. This enables to truncate such infinite sums (which all involve factors f_n) to only the finite set of occupied orbitals where $f_n > \epsilon_{\text{occ}}$. See [11] for an in depth discussion. Denoting the number of occupied orbitals by $N_{\text{occ}} := \max\{n \in \mathbb{N} \mid f_n > \epsilon_{\text{occ}}\}$ we can express the application of χ_0 as

$$(2.10) \quad \chi_0 \delta V = \sum_{n=1}^{N_{\text{occ}}} 2f_n \text{Re}(\phi_n^* \delta\phi_n) + \delta f_n |\phi_n|^2$$

where $\delta\phi_n$ is the change in the orbital ϕ_n induced by the perturbation δV (detailed below) and δf_n is the change in occupation computed by

$$(2.11) \quad \delta f_n = f'_n \left(\langle \phi_n, \delta V \phi_n \rangle - \delta\epsilon_{\text{F}} \right).$$

Here, $\delta\epsilon_{\text{F}}$ is chosen such that $\sum_{n=1}^{N_{\text{occ}}} \delta f_n = 0$ (charge conservation) and here and henceforth we use the convention

$$(2.12) \quad f'_n := \frac{f_n - f_n}{\epsilon_n - \epsilon_n} = \frac{1}{T} f'_{\text{FD}} \left(\frac{\epsilon_n - \epsilon_{\text{F}}}{T} \right).$$

For obtaining $\delta\phi_n$ a few ways have been discussed in the literature amounting to different gauge choices. Here we follow the minimal gauge approach introduced in [11] with the goal to obtain a numerically stable DFPT solution also for metallic systems. By a partition of unity with

$$(2.13) \quad P = \sum_{n=1}^{N_{\text{occ}}} |\phi_n\rangle\langle\phi_n|, \quad \text{and} \quad Q = I - P = \sum_{n=N_{\text{occ}}+1}^{\infty} |\phi_n\rangle\langle\phi_n|,$$

— respectively the orthogonal projectors onto the occupied subspace $\text{span}\{\phi_n\}_{n=1}^{N_{\text{occ}}}$ and unoccupied subspace $\text{span}\{\phi_n\}_{n=N_{\text{occ}}+1}^{\infty}$ — we decompose $\delta\phi_n$ into two contributions $\delta\phi_n = P\delta\phi_n + Q\delta\phi_n$. For each $n = 1, \dots, N_{\text{occ}}$ the first term is computed via an explicit sum over states

$$(2.14) \quad \delta\phi_n^P := P\delta\phi_n = \sum_{m=1}^{N_{\text{occ}}} \frac{f_n^2}{f_n^2 + f_m^2} \frac{f_n - f_m}{\epsilon_n - \epsilon_m} \langle \phi_m, \delta V \phi_n \rangle \phi_m.$$

while the second term is computed by solving the Sternheimer equations (SE)

$$(2.15) \quad Q(H_\rho - \epsilon_n)Q\delta\phi_n^Q = -Q(\delta V\phi_n)$$

for $\delta\phi_n^Q := Q\delta\phi_n$. See [11] for a detailed derivation of the above expressions.

2.3. Numerical Discretisation.

2.3.1. Plane-wave basis sets and Fourier transforms. In this section we provide a description of plane-wave basis sets and Fourier transforms, including key details that will be important for our development of adaptive Sternheimer tolerance strategies. A deeper theoretical or computational discussion of these standard results can be found in [42, 10, 6].

In periodic systems the unknown functions are \mathbb{L} -periodic and thus can be approximated using a Fourier basis. We use normalised plane waves, defined as $e_{\mathbf{G}}(\mathbf{r}) = e^{i\mathbf{G}\cdot\mathbf{r}}/\sqrt{|\Omega|}$ where $|\Omega|$ is the volume of the unitcell Ω and $\mathbf{G} \in \mathbb{L}^*$. To represent densities and orbitals to consistent approximation a larger basis set is employed for densities [6, 42]. We define the spherical Fourier basis \mathcal{X}° (for orbitals) and the cubic Fourier basis \mathcal{X}^\square (for densities) by

$$(2.16) \quad \begin{aligned} \mathcal{X}^\circ &:= \text{span}\{e_{\mathbf{G}} \mid \mathbf{G} \in \mathbb{G}^\circ\} \text{ with } \mathbb{G}^\circ := \left\{ \mathbf{G} \in \mathbb{L}^* \mid \|\mathbf{G}\|_2 \leq \sqrt{2E_{\text{cut}}} \right\}, \\ \mathcal{X}^\square &:= \text{span}\{e_{\mathbf{G}} \mid \mathbf{G} \in \mathbb{G}^\square\} \text{ with } \mathbb{G}^\square := \left\{ \mathbf{G} \in \mathbb{L}^* \mid \|\mathbf{G}\|_\infty \leq 2\sqrt{2E_{\text{cut}}} \right\}, \end{aligned}$$

respectively. Here, the cut-off energy $E_{\text{cut}} > 0$ is a user-defined parameter. The dimension of these sets are

$$(2.17) \quad \begin{aligned} N_b &:= \dim \mathcal{X}^\circ = |\mathbb{G}^\circ| = C_d \frac{4\pi}{3} \left(\sqrt{2E_{\text{cut}}} \right)^3 \simeq \frac{\sqrt{2}}{3\pi^2} E_{\text{cut}}^{3/2} |\Omega|, \\ N_g &:= \dim \mathcal{X}^\square = |\mathbb{G}^\square| = C_d \left(4\sqrt{2E_{\text{cut}}} \right)^3 \simeq \frac{16\sqrt{2}}{\pi^3} E_{\text{cut}}^{3/2} |\Omega|, \end{aligned}$$

where $C_d \simeq |\Omega|/(2\pi)^3$ is the (average) number of lattice points per unit volume in the reciprocal lattice \mathbb{L}^* .

The discretised orbitals and electron density, denoted by the bold font ϕ_n° and ρ^\square , are vectors in \mathbb{C}^{N_b} and \mathbb{C}^{N_g} containing the Fourier coefficients

$$(2.18) \quad \begin{aligned} \phi_n^\circ &:= [\widehat{\phi_n}]_{\mathbf{G} \in \mathbb{G}^\circ} \in \mathbb{C}^{N_b}, \quad \phi_n(\mathbf{r}) \approx \sum_{\mathbf{G} \in \mathbb{G}^\circ} [\widehat{\phi_n}]_{\mathbf{G}} e_{\mathbf{G}}(\mathbf{r}) \in \mathcal{X}^\circ, \\ \rho^\square &:= [\widehat{\rho}]_{\mathbf{G} \in \mathbb{G}^\square} \in \mathbb{C}^{N_g}, \quad \rho(\mathbf{r}) \approx \sum_{\mathbf{G} \in \mathbb{G}^\square} [\widehat{\rho}]_{\mathbf{G}} e_{\mathbf{G}}(\mathbf{r}) \in \mathcal{X}^\square, \end{aligned}$$

respectively. Note that with our normalisation convention the Fourier coefficients $[\widehat{u}]_{\mathbf{G}}$ of a function $u(\mathbf{r}) \in L_\Omega^2(\mathbb{R}^3, \mathbb{C})$ are obtained as $[\widehat{u}]_{\mathbf{G}} = \langle e_{\mathbf{G}}, u \rangle_{L_\Omega^2(\mathbb{R}^3, \mathbb{C})}$.

The reciprocal space grid \mathbb{G}^\square (2.17) can equivalently be expressed as

$$(2.19) \quad \mathbb{G}^\square = \left\{ i_1 \mathbf{b}_1 + i_2 \mathbf{b}_2 + i_3 \mathbf{b}_3 \mid -\frac{N_g^x}{2} \leq i_1 < \frac{N_g^x}{2}, -\frac{N_g^y}{2} \leq i_2 < \frac{N_g^y}{2}, -\frac{N_g^z}{2} \leq i_3 < \frac{N_g^z}{2} \right\},$$

using even integers N_g^x, N_g^y, N_g^z . By means of the inverse Fourier transform (FT) Fourier coefficients are mapped to values on the respective real-space grid

$$(2.20) \quad \mathbb{X} := \left\{ \frac{i_1}{N_g^x} \mathbf{a}_1 + \frac{i_2}{N_g^y} \mathbf{a}_2 + \frac{i_3}{N_g^z} \mathbf{a}_3 \mid 0 \leq i_1 < N_g^x, 0 \leq i_2 < N_g^y, 0 \leq i_3 < N_g^z \right\}.$$

continuous objects

discretised objects

$$\begin{array}{ccc}
\phi_n, \delta\phi_n^P, \delta\phi_n^Q & \xrightarrow{\text{discretise in } \mathcal{X}^\circ} & \phi_n, \delta\phi_n^P, \delta\phi_n^Q \in \mathbb{C}^{N_b} \\
P, Q, H_\rho & & \mathbf{P}, \mathbf{Q}, \mathbf{H}_\rho \in \mathbb{C}^{N_b \times N_b} \\
\\
\rho, \delta\rho, \delta V & \xrightarrow{\text{discretise in } \mathbb{X}} & \rho, \delta\rho, \delta V \in \mathbb{R}^{N_g} \\
\chi_0, K_\rho^{\text{Hxc}}, \mathcal{E} & & \chi_0, \mathbf{K}, \mathbf{\mathcal{E}} \in \mathbb{R}^{N_g \times N_g}
\end{array}$$

Fig. 1: discretisation of continuous objects in the plane-wave basis sets.

For example, denoting by $\mathbf{W} \in \mathbb{C}^{N_g \times N_g}$ the unitary discrete Fourier transform matrix and introducing the weights $w = \sqrt{|\Omega|}/\sqrt{N_g}$ the inverse FT is given by $w^{-1}\mathbf{W}^{-1}$. It maps the Fourier coefficients ρ^\square to function values $\rho(\mathbf{r})$ on the grid \mathbb{X} . The normalisation factor w in this expression is chosen such that the values obtained by an inverse FT are indeed the unscaled function values. Note, the value of the normalisation factor w varies across different software packages. The convention taken here is the one of DFTK [33].

To achieve the same transformation for the orbitals $\phi_n(\mathbf{r})$ — which are only represented on the (smaller) spherical grid \mathbb{G}° — we first pad ϕ_n° with zeros to get ϕ_n^\square and only then apply the inverse FT. Specifically, let $\mathbf{Z} \in \mathbb{C}^{N_g \times N_b}$ be the zero-padding matrix, the transformations from real space function values to the Fourier coefficients on the spherical grid (and vice versa) are given by:

$$\begin{aligned}
(2.21) \quad \mathbf{F} &:= w\mathbf{Z}^\top \mathbf{W} : \mathbb{C}^{N_g} \rightarrow \mathbb{C}^{N_b}, [u(\mathbf{r})]_{\mathbf{r} \in \mathbb{X}} \mapsto [\widehat{u}]_{\mathbf{G} \in \mathbb{G}^\circ}, \\
\mathbf{F}^{-1} &:= w^{-1}\mathbf{W}^{-1}\mathbf{Z} : \mathbb{C}^{N_b} \rightarrow \mathbb{C}^{N_g}, [\widehat{u}]_{\mathbf{G} \in \mathbb{G}^\circ} \mapsto [u(\mathbf{r})]_{\mathbf{r} \in \mathbb{X}},
\end{aligned}$$

which can be implemented efficiently by leveraging the FFT algorithm.

2.3.2. Notation for discretised quantities. In this paper, we use the following conventions for denoting discretised quantities. In general, we use bold font of the same letter to denote the corresponding discretised object. Quantities related to orbitals ($\phi_n, \delta\phi_n, H_\rho$) are by default discretised in the spherical Fourier basis $\mathcal{X}_{E_{\text{cut}}}^\circ$ and quantities related to electron density and potentials ($\rho, \delta\rho, V, \delta V, \chi_0$) are by default discretised in real space \mathbb{X} . Therefore, we may omit the superscripts \circ and \square of the quantities in the following discussions for simplicity. See Figure 1 for a summary of notations. Note that if we let $\Phi = [\phi_1, \dots, \phi_{N_{\text{occ}}}] \in \mathbb{C}^{N_b \times N_{\text{occ}}}$ be the matrix of occupied orbitals, then the projectors P and Q can be written as $\mathbf{P} = \Phi\Phi^\text{H}$ and $\mathbf{Q} = \mathbf{I}_{N_b} - \mathbf{P}$ respectively. We also remark that the orbitals are *orthonormal* in the Fourier basis, i.e., $\Phi^\text{H}\Phi = \mathbf{I}_{N_{\text{occ}}}$ but are only *orthogonal* in the real space due to the normalisation factor w .

2.3.3. Discretised Kohn-Sham equations. Given the above setup, the discretised Kohn-Sham equations (c.f. (2.3)) can be written as

$$(2.22) \quad \mathbf{H}_\rho \phi_n = \epsilon_n \phi_n, \quad n = 1, \dots, N_{\text{occ}}, \quad \langle \phi_n, \phi_m \rangle = \delta_{nm}, \quad \rho = \sum_{n=1}^{N_{\text{occ}}} f_n |\mathbf{F}^{-1} \phi_n|^2,$$

where for the computation of ρ , we first transform the orbitals to real space by the inverse FT and then sum up the modulus squares of the transformed orbitals. Note

that the operation $|\cdot|^2$ should be understood component-wise. This non-linear eigenvalue problem is usually solved by the *self-consistent field* (SCF) iterations yielding N_{occ} eigenpairs

$$(2.23) \quad (\epsilon_n, \phi_n) \in \mathbb{R} \times \mathbb{C}^{N_b} \quad \text{for } n = 1, \dots, N_{\text{occ}},$$

as well as the electron density $\rho \in \mathbb{R}^{N_g}$ and the Hamiltonian matrix $\mathbf{H}_\rho \in \mathbb{C}^{N_b \times N_b}$.

2.3.4. Discretised Dyson equation. With the Kohn-Sham equations (2.22) solved and all these quantities at hand we can write down the discretised Dyson equation as (c.f. (2.8))

$$(2.24) \quad \text{Seek } \delta\rho \in \mathbb{R}^{N_g} \text{ such that } \mathcal{E}\delta\rho = \delta\rho_0,$$

where $\mathcal{E} := \mathbf{I}_{N_g} - \chi_0 \mathbf{K} \in \mathbb{R}^{N_g \times N_g}$, $\delta\rho_0 := \chi_0 \delta \mathbf{V}_0 \in \mathbb{R}^{N_g}$. The dielectric adjoint \mathcal{E} is accessed through the matrix-vector product (c.f. (2.10))

$$(2.25) \quad \mathcal{E}\mathbf{v} = \mathbf{v} - \|\mathbf{K}\mathbf{v}\| \sum_{n=1}^{N_{\text{occ}}} 2f_n \text{Re} \left((\mathbf{F}^{-1}\phi_n)^* \odot (\mathbf{F}^{-1}\delta\phi_n^P + \mathbf{F}^{-1}\delta\phi_n^Q) \right) + \delta f_n |\mathbf{F}^{-1}\phi_n|^2,$$

where for $n = 1, \dots, N_{\text{occ}}$, occupied variations $\delta\phi_n^P \in \mathbb{C}^{N_b}$ are computed explicitly by a sum over states (c.f. (2.14))

$$(2.26) \quad \delta\phi_n^P = \sum_{m=1}^{N_{\text{occ}}} \frac{f_n^2}{f_n^2 + f_m^2} \frac{f_n - f_m}{\epsilon_n - \epsilon_m} \langle \phi_m, \mathbf{F}((\mathbf{K}\mathbf{v}) \odot (\mathbf{F}^{-1}\phi_n)) \rangle \phi_m / \|\mathbf{K}\mathbf{v}\|,$$

the unoccupied variations $\delta\phi_n^Q \in \mathbb{C}^{N_b}$ are computed by solving the discretised SE (c.f. (2.15))

$$(2.27) \quad \mathbf{Q}(\mathbf{H}_\rho - \epsilon_n \mathbf{I}_{N_b}) \mathbf{Q} \delta\phi_n^Q = -\mathbf{Q}\mathbf{F}((\mathbf{K}\mathbf{v}) \odot (\mathbf{F}^{-1}\phi_n)) / \|\mathbf{K}\mathbf{v}\|,$$

and the occupation changes δf_n are computed by $\delta f_n = f'_n (\delta\epsilon_n - \delta\epsilon_F)$ with $\delta\epsilon_n = \langle \phi_n, \mathbf{F}((\mathbf{K}\mathbf{v}) \odot (\mathbf{F}^{-1}\phi_n)) \rangle / \|\mathbf{K}\mathbf{v}\|$ and $\delta\epsilon_F, f'_n$ as described in Section 2.2.

Here, the operations Re , \odot , $*$, and $|\cdot|^2$ in (2.25) should be understood component-wise. In particular, \odot denotes the Hadamard product. Note, that this formulation exploits the linearity of χ_0 to rewrite $\mathcal{E}\mathbf{v} = \mathbf{v} - \|\mathbf{K}\mathbf{v}\| \chi_0(\mathbf{K}\mathbf{v} / \|\mathbf{K}\mathbf{v}\|)$ explaining the appearance of terms $\|\mathbf{K}\mathbf{v}\|$ in the above expressions. This ensures the RHS of (2.27) to remain within a reasonable numerical range even if $\|\mathbf{K}\mathbf{v}\|$ happens to be small, which renders solving (2.27) numerically more stable.

2.3.5. Structure of the Dyson equation and typical numerical algorithms. Recall that $N_g \approx 16N_b$ (see (2.17)). Therefore in plane-wave bases the Dyson equation is a large $N_g \times N_g$ *real non-symmetric* linear system, while the SE is a *complex Hermitian* linear system with a smaller size $N_b \times N_b$. Both the dielectric adjoint \mathcal{E} and the Hamiltonian \mathbf{H}_ρ are not explicitly formed and are only accessed through matrix-vector products to benefit from an efficient FFT-based evaluation. Both the Dyson and Sternheimer equations are thus solved using iterative methods.

We use the generalised minimal residual (GMRES) method [49] for the Dyson equation and the conjugate gradient (CG) [34] method for the SEs. This results in a nested problem: at the i -th GMRES iteration, an application of \mathcal{E} to a Krylov basis vector is required, which in turn requires the iterative solution of N_{occ} SEs by CG with some tolerance $\tau_{i,n}^{\text{CG}}$ for $n = 1, \dots, N_{\text{occ}}$. Selecting the appropriate CG tolerances is crucial for the efficiency and accuracy of the solution of the Dyson equation, which will be discussed in the following sections.

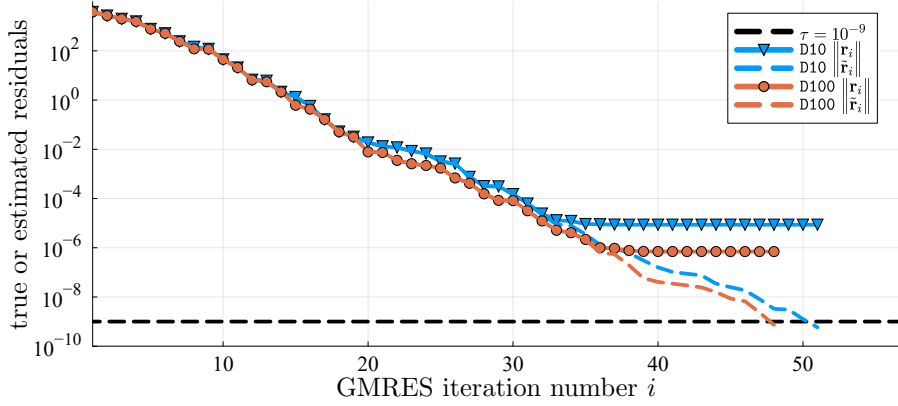


Fig. 2: True residuals $\|\mathbf{r}_i\|$ (solid lines) and estimated residuals $\|\tilde{\mathbf{r}}_i\|$ (dashed lines) v.s. GMRES iteration for system in Section 2.3.5. The baseline strategies $\tau_{i,n}^{\text{CG}} = \tau/10, \tau/100$ (D10, D100) are used for the CG solvers for the SEs.

3. An inexact preconditioned GMRES method for the Dyson equation.

3.1. Why a naive static tolerance selection can fail. We first illustrate the deficiencies of a naive GMRES approach, which solves the Dyson equation $\mathcal{E}\delta\rho = \delta\rho_0$ employing simply a static threshold $\tau_{i,n}^{\text{CG}}$ for the inner SE problems. Given an initial guess $\mathbf{x}_0 \in \mathbb{R}^{N_g}$ to the solution $\delta\rho$, GMRES generates a sequence of approximations $\mathbf{x}_m = \mathbf{x}_0 + \mathbf{V}_m \mathbf{y}_m$ such that \mathbf{y}_m minimises the ℓ_2 norm of the residual $\mathbf{r}_m := \delta\rho_0 - \mathcal{E}\mathbf{x}_m$. Here, $\mathbf{V}_m = [\mathbf{v}_1, \mathbf{v}_2, \dots, \mathbf{v}_m] \in \mathbb{R}^{N_g \times m}$ is the orthonormal basis of the Krylov subspace $\mathcal{K}_m(\mathcal{E}, \mathbf{b})$ and satisfies the Arnoldi decomposition $\mathcal{E}\mathbf{V}_m = \mathbf{V}_{m+1}\mathbf{H}_m$ where $\mathbf{H}_m \in \mathbb{R}^{(m+1) \times m}$ is an upper Hessenberg matrix. $\mathbf{y}_m \in \mathbb{R}^m$ are the coefficients in the basis \mathbf{V}_m , determined by solving the $N_g \times m$ least squares (LS) problem $\mathbf{y}_m := \min_{\mathbf{y} \in \mathbb{R}^m} \|\delta\rho_0 - \mathcal{E}(\mathbf{x}_0 + \mathbf{V}_m \mathbf{y})\|$, which due to the Arnoldi decomposition is equivalent to the $(m+1) \times m$ LS problem

$$(3.1) \quad \mathbf{y}_m = \min_{\mathbf{y} \in \mathbb{R}^m} \|\beta \mathbf{e}_1 - \mathbf{H}_m \mathbf{y}\|,$$

where $\beta = \|\mathbf{r}_0\|$ and \mathbf{e}_1 is the first column of the conformable identity matrix. Let the *estimated residual* be $\tilde{\mathbf{r}}_m := \beta \mathbf{e}_1 - \mathbf{H}_m \mathbf{y}_m$ then GMRES terminates when $\|\tilde{\mathbf{r}}_m\|$ is below a tolerance τ since $\|\mathbf{r}_m\| = \|\tilde{\mathbf{r}}_m\| \leq \tau$. However, the first equality is only true when the matrix-vector products $\mathcal{E}\mathbf{v}_i$ are computed *exactly*. In our nested linear problem setting this is not the case as we only solve the inner SEs to finite tolerance. We make this explicit by denoting the inexact matrix-vector product as $\tilde{\mathcal{E}}^{(i)} \mathbf{v}_i \approx \mathcal{E}\mathbf{v}_i$ at the i -th GMRES iteration. As a consequence only the *inexact* Arnoldi decomposition

$$(3.2) \quad [\tilde{\mathcal{E}}^{(1)} \mathbf{v}_1, \tilde{\mathcal{E}}^{(2)} \mathbf{v}_2, \dots, \tilde{\mathcal{E}}^{(m)} \mathbf{v}_m] = \mathbf{V}_{m+1} \mathbf{H}_m$$

holds during the GMRES, such that $\|\mathbf{r}_m\| \neq \|\tilde{\mathbf{r}}_m\|$. The usual termination criterion $\|\tilde{\mathbf{r}}_m\| \leq \tau$ may thus *not* guarantee $\|\mathbf{r}_m\| \leq \tau$.

This is illustrated in Figure 2 for solving the Dyson equation (with no preconditioner) for an aluminium bulk system with 40 atoms, see Section 4.2 for details of the experimental setup. We consider two baseline strategies D10 and D100, in which we set the tolerances of the CG solvers for all SEs to be the desired GMRES accuracy τ

divided by a constant factor 10 or 100, respectively. In the notation of Section 2.3.5 we thus set $\tau_{i,n}^{\text{CG}} = \tau/10$ or $\tau_{i,n}^{\text{CG}} = \tau/100$. Both the estimated norms $\|\tilde{\mathbf{r}}_i\|$ (accessible during the GMRES procedure) and the true residual norms $\|\mathbf{r}_i\|$ (computed explicitly by using tight SE tolerances $\tau_{i,n}^{\text{CG}} = 10^{-16}$) are shown in Figure 2 for $\tau = 10^{-9}$. Initially the estimated residuals match the true residuals. However, around iteration 35 we observe a deviation of both quantities: while the estimated residuals keep decreasing, the true residuals stagnate. At convergence, i.e. when $\|\tilde{\mathbf{r}}_i\| \leq \tau$, the returned solution turns out to be at least 3 orders of magnitude less accurate than τ .

In this work we will develop adaptive strategies for choosing the CG tolerances $\tau_{i,n}^{\text{CG}}$, which will not only cure this deficiency, but also bring computational savings compared to choosing $\tau_{i,n}^{\text{CG}}$ statically across all GMRES iterations.

3.2. Theoretical analysis of the inexact GMRES method for the Dyson equation. Krylov subspace methods with inexact matrix-vector products have been studied in the literature, see [50, 52]. A key result is the following lemma, which provides a bound of the true residual by the estimated residual and the error in the inexact matrix-vector products $(\tilde{\mathcal{E}}^{(i)} - \mathcal{E})\mathbf{v}_i$.

LEMMA 3.1. *Given the notations developed above, we have*

$$(3.3) \quad \|\mathbf{r}_m\| \leq \|\mathbf{E}_0\mathbf{x}_0\| + \|\tilde{\mathbf{r}}_m\| + \sum_{i=1}^m \|\mathbf{E}_i\mathbf{v}_i\| \|\mathbf{y}_m\|_i,$$

where $\mathbf{E}_i := \tilde{\mathcal{E}}^{(i)} - \mathcal{E}$ is the error matrix at the i -th GMRES iteration and $[\mathbf{y}_m]_i$ is the i -th element of the vector \mathbf{y}_m defined in (3.1).

This result is a restatement of [50, Proposition 4.1] adapted to our notation. The behaviour of $\|\mathbf{y}_m\|_i$ is also well-understood and can in fact be bounded by the estimated residual of the previous iteration $\|\tilde{\mathbf{r}}_{i-1}\|$:

LEMMA 3.2 ([50], Lemma 5.1). *Given \mathbf{y}_m as in (3.1), we have*

$$(3.4) \quad \|\mathbf{y}_m\|_i \leq \frac{1}{\sigma_m(\mathbf{H}_m)} \|\tilde{\mathbf{r}}_{i-1}\|, \quad \text{for } i = 1, 2, \dots, m,$$

where $\sigma_m(\cdot)$ is the m -th singular value of a matrix sorted in descending order.

For completeness we provide proofs of both results in Appendix A. Notably a simpler proof of Lemma 3.2 compared to the original one in [50] is given. Combining Lemmas 3.1 and 3.2 immediately yields the following theorem.

THEOREM 3.3. *For any tolerance $\tau > 0$, if the error matrices $\mathbf{E}_0, \dots, \mathbf{E}_m$ satisfy*

$$(3.5) \quad \|\mathbf{E}_0\mathbf{x}_0\| \leq c_0\tau, \quad \|\mathbf{E}_i\mathbf{v}_i\| \leq c_i \frac{\sigma_m(\mathbf{H}_m)}{\|\tilde{\mathbf{r}}_{i-1}\|} \tau, \quad \text{for } i = 1, 2, \dots, m,$$

and the estimated residual norm $\|\tilde{\mathbf{r}}_m\| \leq c_{m+1}\tau$, for some constants $c_0, \dots, c_{m+1} > 0$ such that $\sum_{i=0}^{m+1} c_i \leq 1$, then the method terminates at the m -th iteration with the accuracy τ , i.e., $\|\mathbf{r}_m\| \leq \tau$.

The estimated residual norm $\|\tilde{\mathbf{r}}_i\|$ is monotonically decreasing. Therefore, Theorem 3.3 suggests that we can be *increasingly crude* when computing the approximate matrix-vector products $\tilde{\mathcal{E}}^{(i)}\mathbf{v}_i$ as the iteration proceeds. As a result larger CG tolerances $\tau_{i,n}^{\text{CG}}$ can be employed, thereby saving computational cost. Based on Theorem 3.3 we propose the following inexact GMRES algorithm.

Algorithm 3.1 Inexact GMRES(m)

Require: $\mathcal{E} \in \mathbb{C}^{N_g \times N_g}$, $\mathbf{b} \in \mathbb{C}^{N_g}$, $\mathbf{x}_0 \in \mathbb{C}^{N_g}$, restart size $m \in \mathbb{N}$, tolerance $\tau > 0$; initial guess s of $\sigma_m(\mathbf{H}_m)$, a procedure that given any error $\tau' > 0$ and a vector $\mathbf{v} \in \mathbb{C}^{N_g}$ returns an inexact matrix-vector product $\tilde{\mathcal{E}}\mathbf{v}$ such that $\|(\mathcal{E} - \tilde{\mathcal{E}})\mathbf{v}\| \leq \tau'$.

Ensure: An approximate solution \mathbf{x} with $\|\mathbf{b} - \mathcal{E}\mathbf{x}\| \leq \tau$

- 1: Compute $\mathbf{r}_0 = \mathbf{b} - \tilde{\mathcal{E}}^{(0)}\mathbf{x}_0$ with $\|(\mathcal{E} - \tilde{\mathcal{E}}^{(0)})\mathbf{x}_0\| \leq \tau/3$
- 2: $\beta = \|\mathbf{r}_0\|$, $\mathbf{v}_1 = \mathbf{r}_0/\beta$, $\mathbf{V}_1 = \mathbf{v}_1$, $\mathbf{H}_0 = [\]$, $\|\tilde{\mathbf{r}}_0\| = \beta$
- 3: **for** $i = 1, 2, \dots, m$ **do**
- 4: Compute $\mathbf{w} = \tilde{\mathcal{E}}^{(i)}\mathbf{v}_i$ with $\|(\mathcal{E} - \tilde{\mathcal{E}}^{(i)})\mathbf{v}_i\| \leq \frac{s}{3m} \frac{1}{\|\tilde{\mathbf{r}}_{i-1}\|} \tau$
- 5: Build \mathbf{V}_{i+1} , \mathbf{H}_i by Arnoldi process, compute the estimated residual $\|\tilde{\mathbf{r}}_i\|$
- 6: **if** $\|\tilde{\mathbf{r}}_i\| \leq \tau/3$ **then**
- 7: Compute $\sigma_k(\mathbf{H}_k)$; Compute \mathbf{y}_k , $\mathbf{x} = \mathbf{x}_0 + \mathbf{V}_i\mathbf{y}_i$
- 8: **if** $s \leq \sigma_k(\mathbf{H}_k)$ **then return** \mathbf{x}
- 9: **if** $s > \sigma_k(\mathbf{H}_k)$ **then Restart:** $s = \sigma_k(\mathbf{H}_k)$, $\mathbf{x}_0 = \mathbf{x}$, go to Line 1
- 10: **if** $\|\tilde{\mathbf{r}}_m\| > \tau/3$ **then**
- 11: Compute $\sigma_m(\mathbf{H}_m)$; Compute \mathbf{y}_m , $\mathbf{x} = \mathbf{x}_0 + \mathbf{V}_m\mathbf{y}_m$
- 12: Restart: $s = \sigma_m(\mathbf{H}_m)$, $\mathbf{x}_0 = \mathbf{x}$, go to Line 1

Compared to the original work [50] our version of inexact GMRES employs an adaptive strategy to estimate the m -th singular value $\sigma_m(\mathbf{H}_m)$ of the Hessenberg matrix. Note that $\sigma_m(\mathbf{H}_m)$ in bound (3.5) is only available *after* the m -th iteration and thus cannot be computed in practice. Here, we propose to introduce a variable s , which gets updated along with the GMRES iterations, such that at convergence s is ensured to be a lower bound to $\sigma_m(\mathbf{H}_m)$. Concretely we change s under two circumstances. First, during a normal restart of the GMRES after m iterations. Then we set s to the smallest singular value so far encountered, $s = \sigma_m(\mathbf{H}_m)$ (line 12). Second, if convergence of the GMRES is flagged by the estimated residual norm (line 6), but s happens to overestimate $\sigma_k(\mathbf{H}_k)$ — implying that the assumptions of Theorem 3.3 are violated. In such a case we perform an additional restart, updating s again to the smallest singular value of the Hessenberg matrix, see line 9. After this additional restart the GMRES convergence criterion in line 6 is quickly re-achieved (usually just one or two GMRES iterations), but this time satisfying $s \leq \sigma_k(\mathbf{H}_k)$, such that the algorithm terminates. While such additional restarts are rare, they guarantee that (3.5) and thus that $\|\mathbf{r}_m\| < \tau$ are satisfied — such that we obtain the prescribed accuracy despite employing inexact matrix-vector products.

This strategy for handling the unknown singular values $\sigma_m(\mathbf{H}_m)$ in the context of inexact GMRES appears to be novel, despite being a natural refinement of well-established ideas in inexact GMRES.

Remark 3.4. For simplicity, in Algorithm 3.1 we chose an equal distribution of error between the three terms of (3.3), i.e., $c_0 = c_{m+1} = 1/3$ and $c_1 = \dots = c_m = 1/(3m)$ in Theorem 3.3.

The missing ingredient to apply this inexact GMRES procedure to the Dyson equation is a recipe for choosing the CG tolerances $\tau_{i,n}^{\text{CG}}$ in a way that the error $\|(\mathcal{E} - \tilde{\mathcal{E}}^{(i)})\mathbf{v}_i\|$ stays below the bound in line 4 of Algorithm 3.1. First note that the

inexact matrix-vector product $\tilde{\mathcal{E}}^{(i)} \mathbf{v}_i$ is computed by

$$(3.6) \quad \begin{aligned} \mathcal{E} \mathbf{v}_i &\approx \tilde{\mathcal{E}}^{(i)} \mathbf{v}_i \\ &= \mathbf{v}_i - \|\mathbf{K} \mathbf{v}_i\| \sum_{n=1}^{N_{\text{occ}}} 2f_n \operatorname{Re} \left((\mathbf{F}^{-1} \phi_n)^* \odot (\mathbf{F}^{-1} \delta \phi_n^P + \mathbf{F}^{-1} \widetilde{\delta \phi_n^Q}^{(i)}) \right) + \delta f_n |\mathbf{F}^{-1} \phi_n|^2, \end{aligned}$$

that is (2.25), where instead of the exact SE solutions $\delta \phi_n^Q$ one employs the approximate orbital responses $\widetilde{\delta \phi_n^Q}^{(i)}$. Introducing the shorthands

$$(3.7) \quad \underbrace{\mathbf{Q} (\mathbf{H}_\rho - \epsilon_n \mathbf{I}_{N_b}) \mathbf{Q}}_{=: \mathbf{A}_n} \delta \phi_n^Q = - \underbrace{\mathbf{Q} \mathbf{F} ((\mathbf{K} \mathbf{v}_i) \odot (\mathbf{F}^{-1} \phi_n))}_{=: \mathbf{b}_n^{(i)}} / \|\mathbf{K} \mathbf{v}_i\|$$

for (2.27) the relationship between the approximate orbital responses and the CG tolerances $\tau_{i,n}^{\text{CG}}$ is thus $\|\mathbf{b}_n^{(i)} - \mathbf{A}_n \widetilde{\delta \phi_n^Q}^{(i)}\| \leq \tau_{i,n}^{\text{CG}}$. With this notation the following lemma provides the desired bound.

LEMMA 3.5. *The error of the application of the inexact dielectric adjoint $\tilde{\mathcal{E}}^{(i)}$ on a vector $\mathbf{v}_i \in \mathbb{R}^{N_g}$ is bounded by*

$$(3.8) \quad \|(\mathcal{E} - \tilde{\mathcal{E}}^{(i)}) \mathbf{v}_i\| \leq 2 \|\mathbf{K} \mathbf{v}_i\| \|\operatorname{Re}(\mathbf{F}^{-1} \Phi)\|_{2,\infty} \frac{\sqrt{N_g N_{\text{occ}}}}{\sqrt{|\Omega|}} \max_{n=1, \dots, N_{\text{occ}}} \frac{f_n}{\epsilon_{N_{\text{occ}}+1} - \epsilon_n} \tau_{i,n}^{\text{CG}},$$

where $\|\mathbf{M}\|_{2,\infty} := \max_{i=1, \dots, n} \|\mathbf{M}_{i,:}\|_2$ is the maximum row norm for $\mathbf{M} \in \mathbb{C}^{n \times n}$, see e.g. [40] for the justification of this notation.

Proof of Lemma 3.5. Recall that $\Phi \in \mathbb{C}^{N_b \times N_{\text{occ}}}$ contains the eigenvectors of \mathbf{H}_ρ with eigenvalues $\epsilon_1, \dots, \epsilon_{N_{\text{occ}}}$. Let $\Phi_\perp \in \mathbb{C}^{N_b \times (N_b - N_{\text{occ}})}$ be the orthonormal matrix whose columns are the eigenvectors of \mathbf{H}_ρ with eigenvalues $\epsilon_{N_{\text{occ}}+1}, \dots, \epsilon_{N_b}$. Note that this construction does not imply that the full eigendecomposition of \mathbf{H}_ρ is indeed computed in practice. Then we have $\mathbf{Q} = \Phi_\perp \Phi_\perp^H$. Let $\mathbf{D}_n = \operatorname{diag}(\epsilon_{N_{\text{occ}}+1} - \epsilon_n, \dots, \epsilon_{N_b} - \epsilon_n) \in \mathbb{R}^{(N_b - N_{\text{occ}}) \times (N_b - N_{\text{occ}})}$ be a diagonal matrix. Then direct manipulation yields $\mathbf{A}_n = \Phi_\perp \mathbf{D}_n \Phi_\perp^H$, and thus $\mathbf{A}_n^\dagger = \Phi_\perp \mathbf{D}_n^{-1} \Phi_\perp^H$, where \mathbf{A}_n^\dagger denotes the pseudo-inverse of \mathbf{A}_n in (3.7). Note, that this assumes a gap $\epsilon_{N_{\text{occ}}+1} - \epsilon_{N_{\text{occ}}} > 0$, which is always true in the discretised setting. Hence we have $\mathbf{A}_n^\dagger \mathbf{A}_n = \mathbf{A}_n \mathbf{A}_n^\dagger = \mathbf{Q}$. An exact solution of (3.7) is given by $\delta \phi_n^Q = \mathbf{A}_n^\dagger \mathbf{b}_n^{(i)} \in \operatorname{range}(\mathbf{Q})$.

Since $\mathbf{b}_n^{(i)} \in \operatorname{range}(\mathbf{Q})$, therefore the Krylov subspace $\mathcal{K}_k(\mathbf{A}_n, \mathbf{b}_n^{(i)})$ is contained in $\operatorname{range}(\mathbf{Q})$, and therefore the approximate solution $\widetilde{\delta \phi_n^Q}^{(i)}$ produced by the CG algorithm applied to (3.7) is also in $\operatorname{range}(\mathbf{Q})$. We have

$$(3.9) \quad \begin{aligned} \mathbf{z}_n^{(i)} &:= \delta \phi_n^Q - \widetilde{\delta \phi_n^Q}^{(i)} = \mathbf{Q} (\delta \phi_n^Q - \widetilde{\delta \phi_n^Q}^{(i)}) \\ &= \mathbf{A}_n^\dagger \mathbf{A}_n (\delta \phi_n^Q - \widetilde{\delta \phi_n^Q}^{(i)}) = \mathbf{A}_n^\dagger (\mathbf{b}_n^{(i)} - \mathbf{A}_n \widetilde{\delta \phi_n^Q}^{(i)}). \end{aligned}$$

Furthermore,

$$(3.10) \quad \|\mathbf{z}_n^{(i)}\| \leq \|\mathbf{A}_n^\dagger\| \|\mathbf{b}_n^{(i)} - \mathbf{A}_n \widetilde{\delta \phi_n^Q}^{(i)}\| \leq \frac{1}{\epsilon_{N_{\text{occ}}+1} - \epsilon_n} \tau_{i,n}^{\text{CG}}.$$

Combine (2.25), (3.6) and define $\mathbf{Y} := [f_1 \mathbf{z}_1^{(i)}, \dots, f_n \mathbf{z}_n^{(i)}] \in \mathbb{C}^{N_b \times N_{\text{occ}}}$, we have

$$\begin{aligned}
(3.11) \quad \|(\mathcal{E} - \tilde{\mathcal{E}}^{(i)})\mathbf{v}_i\| &= 2 \|\mathbf{K}\mathbf{v}_i\| \left\| \sum_{n=1}^{N_{\text{occ}}} f_n \text{Re} \left((\mathbf{F}^{-1} \phi_n)^* \odot (\mathbf{F}^{-1} \mathbf{z}_n^{(i)}) \right) \right\| \\
&= 2 \|\mathbf{K}\mathbf{v}_i\| \left\| ((\text{Re}(\mathbf{F}^{-1} \Phi)) \odot (\text{Re}(\mathbf{F}^{-1} \mathbf{Y}))) \cdot \mathbf{1}_{N_{\text{occ}}} \right\| \\
&\leq 2 \|\mathbf{K}\mathbf{v}_i\| \|\text{Re}(\mathbf{F}^{-1} \Phi)\|_{2,\infty} \|\text{Re}(\mathbf{F}^{-1} \mathbf{Y})\|_{1,2} \sqrt{N_{\text{occ}}},
\end{aligned}$$

where $\mathbf{1}_{N_{\text{occ}}} = [1, \dots, 1]^T \in \mathbb{R}^{N_{\text{occ}}}$ and we used [35, Theorem 5.5.3] to bound the norm of the Hadamard product by the product of these two norms. Furthermore $\|\cdot\|_{1,2}$ is the maximum column norm for a matrix (in analogy to $\|\cdot\|_{2,\infty}$). The result then follows from

$$(3.12) \quad \|\text{Re}(\mathbf{F}^{-1} \mathbf{Y})\|_{1,2} \leq \|\mathbf{F}^{-1} \mathbf{Y}\|_{1,2} \leq \|\mathbf{F}^{-1}\| \|\mathbf{Y}\|_{1,2} = w^{-1} \max_{n=1, \dots, N_{\text{occ}}} f_n \|\mathbf{z}_n^{(i)}\|. \quad \square$$

Remark 3.6. We remark here that $\delta\phi_n^{Q(i)} = \mathbf{A}_n^\dagger \mathbf{b}_n^{(i)} \in \text{range}(\mathbf{Q})$ is the unique solution to the SE (3.7) in $\text{range}(\mathbf{Q})$. Otherwise, let $\mathbf{c} \in \text{range}(\mathbf{Q})$ be another solution. Then $\mathbf{A}_n (\mathbf{c} - \delta\phi_n^{Q(i)}) = \mathbf{0}$ and $\mathbf{c} - \delta\phi_n^{Q(i)} = \Phi_\perp \alpha$ for some $\alpha \in \mathbb{C}^{(N_b - N_{\text{occ}})}$.

Therefore $\alpha^H \Phi_\perp^H \mathbf{A}_n \Phi_\perp \alpha = \alpha^H D_n \alpha = 0$, which implies $\alpha = \mathbf{0}$ and thus $\mathbf{c} = \delta\phi_n^{Q(i)}$. Since all iterates (as well as the conjugate gradients, residuals) of CG algorithm all lie in $\text{range}(\mathbf{Q})$, $\delta\phi_n^{Q(i)}$ is thus also the solution that the CG algorithm converges to in exact arithmetic. In practical implementations, each CG iterate (also the conjugate gradient, residual) is projected onto $\text{range}(\mathbf{Q})$ to prevent the loss of orthogonality due to numerical errors. It is also worth noting that the solution to the SE is not unique in the full space, e.g., $\delta\phi_n^{Q(i)} + \Phi \alpha$ for any $\alpha \in \mathbb{C}^{N_{\text{occ}}}$ is also a solution.

Combining Lemma 3.5 with Theorem 3.3 we obtain immediately our main theoretical result.

THEOREM 3.7. *Consider the inexact GMRES method applied to the discretised Dyson equation (2.24) $\mathcal{E}\delta\rho = \delta\rho_0$ and define the prefactor*

$$(3.13) \quad C_{i,n} = \frac{\sqrt{|\Omega|}(\epsilon_{N_{\text{occ}}+1} - \epsilon_n)}{2f_n \|\mathbf{K}\mathbf{v}_i\| \|\text{Re}(\mathbf{F}^{-1} \Phi)\|_{2,\infty} \sqrt{N_g N_{\text{occ}}}}$$

where we understand $\mathbf{v}_0 := \mathbf{x}_0$ (initial guess). For any prescribed accuracy $\tau > 0$, if the tolerance $\tau_{i,n}^{\text{CG}}$ of the Sternheimer equation CG solver satisfies

$$(3.14) \quad \tau_{0,n}^{\text{CG}} \leq C_{0,n} \frac{\tau}{3} \quad \text{and} \quad \tau_{i,n}^{\text{CG}} \leq C_{i,n} \frac{\sigma_m(\mathbf{H}_m)}{3m} \frac{\tau}{\|\tilde{\mathbf{r}}_{i-1}\|}$$

for $i = 1, \dots, m$, $n = 1, \dots, N_{\text{occ}}$ and the estimated residual of the GMRES method satisfies $\|\tilde{\mathbf{r}}_m\| \leq \tau/3$, then the method terminates at the m -th iteration with accuracy τ , i.e., true residual $\|\mathbf{r}_m\| \leq \tau$.

Remark 3.8 (Superlinear convergence). We remark here that with the adaptive CG tolerances chosen according to Theorem 3.7 we can expect the inexact GMRES method applied to the Dyson equation to converge *superlinearly* with respect to the total number of CG iterations. This is demonstrated qualitatively by the following argument. Suppose GMRES converges linearly with respect to the number of CG

iterations $\|\mathbf{r}_i\| \leq k_0^i \|\mathbf{r}_0\|$ for $0 < k_0 < 1$, then $\tau_{i,n}^{\text{CG}} \sim 1/\|\tilde{\mathbf{r}}_{i-1}\| \sim 1/k_0^{i-1}$. Since CG has at least a linear convergence rate with respect to its number of iterations, the number of CG iterations in GMRES step i is $N_i^{\text{CG}} \sim -k_1 \log \tau_{i,n}^{\text{CG}} + k_2 \sim -k_3 i + k_4$. Here and hereafter we assume all k_j 's are different positive constants. Therefore the total number of CG iterations up to the i -th GMRES iteration satisfies $N_{\leq i}^{\text{CG}} \sim -k_5 i^2 + k_6 i$ and thus solving i in terms of $N_{\leq i}^{\text{CG}}$ yields $i \sim \sqrt{k_7 - N_{\leq i}^{\text{CG}}} + k_8$. Finally, we have $\|\mathbf{r}_i\| \sim k_0^{\sqrt{k_7 - N_{\leq i}^{\text{CG}}} + k_8} \|\mathbf{r}_0\|$.

Remark 3.9 (Preconditioning the Dyson equation). From the arguments in Section 2.2 one can view the Dyson equation as a linearisation of the SCF problem (2.6) around fixed-point (ground state) density. As a result we would expect any technique for improving SCF convergence to be transferable to accelerating convergence when solving the Dyson equation — namely by a mere linearization of the entire SCF algorithm itself. For example the GMRES algorithm can be viewed as the linearisation of Anderson-accelerated fixed-point iterations, which is indeed one standard technique to solve SCF problems (also sometimes called Pulay mixing or the DIIS method). For more details on the relationship between Anderson acceleration and GMRES — see e.g. the discussion in [20, 53]. By a similar line of arguments all preconditioning schemes which have been used to accelerate the SCF should also be used within the GMRES when solving the Dyson equation [21] for the same material. Indeed, it is effectively a large spectral condition number of the dielectric adjoint operator $\mathcal{E} := 1 - \chi_0 K_\rho^{\text{Hxc}}$ — a material-dependent quantity — which is responsible to both slow SCF and slow Dyson equation convergence.

In the SCF context the Kerker preconditioner [37] is widely employed. It effectively cures the divergence of the Coulomb operator K_ρ^H for large wavelengths (small $\|G\|$), which in metallic materials is not compensated by the independent particle susceptibility operator χ_0 . It thus causes the condition number of \mathcal{E} to grow with system size [30]. Based on above observations we employ the Kerker preconditioner \mathbf{T} when solving the Dyson equation for large metallic systems, i.e. we solve the preconditioned Dyson equation $\mathbf{T}\mathcal{E}\delta\rho = \mathbf{T}\delta\rho_0$. See Appendix B for the explicit functional form of \mathbf{T} . Notably, it can be shown (Lemma B.1) that the Kerker preconditioner has unit norm and thus that $\|\mathbf{T}(\mathcal{E} - \tilde{\mathcal{E}}^{(i)})\mathbf{v}_i\| \leq \|(\mathcal{E} - \tilde{\mathcal{E}}^{(i)})\mathbf{v}_i\|$. Therefore theorem 3.7 still holds when applied to the preconditioned Dyson equation.

3.3. Practical adaptive strategies. The theoretical choice for the CG tolerances suggested by Theorem 3.7 guarantees the accuracy of the returned solution, but tends to be overly conservative. In our numerical studies we will therefore focus on three modifications of the prefactor $C_{i,n}$ of Theorem 3.7, see Table 1. Ranging from conservative to aggressive we term the resulting strategies **grt** (“guaranteed”), **bal** (“balanced”) and **agr** (“aggressive”) — with **bal** providing the best compromise between efficiency and accuracy in our experiments. A discussion of the approximations underlying these strategies is provided in the onset. For completeness Table 1 also lists the definition of three baseline strategies, in which the CG tolerances is constant across all GMRES iterations. These are modelled after common naive choices to choose the tolerance of the inner Sternheimer problems and will be employed in our numerical experiments for comparison.

3.3.1. Dropping the eigenvalue gaps ($\epsilon_{N_{\text{occ}}+1} - \epsilon_n$). This term arises as a bound to the spectral norm of the pseudoinverse $\|A_n^\dagger\|$, which is used in (3.10) to bound

Adaptive strategies $\tau_{i,n}^{\text{CG}} =$		Approximations		
grt	$\frac{1}{\ \mathbf{K}\mathbf{v}_i\ \ \text{Re}(\mathbf{F}^{-1}\Phi)\ _{2,\infty}}$	$\frac{\sqrt{ \Omega }}{2f_n\sqrt{N_g N_{\text{occ}}}}$	$\frac{\sigma_m(\mathbf{H}_m)}{3m} \frac{\tau}{\ \tilde{\mathbf{r}}_{i-1}\ }$	3.3.1
	$\frac{\sqrt{ \Omega }}{\sqrt{N_{\text{occ}}}}$	$\frac{\sqrt{ \Omega }}{2f_n\sqrt{N_g N_{\text{occ}}}}$	$\frac{\sigma_m(\mathbf{H}_m)}{3m} \frac{\tau}{\ \tilde{\mathbf{r}}_{i-1}\ }$	3.3.1 to 3.3.3
bal		1	$\frac{\sigma_m(\mathbf{H}_m)}{3m} \frac{\tau}{\ \tilde{\mathbf{r}}_{i-1}\ }$	Set $C_{i,n} = 1$
agr				
Baseline strategies $\tau_{i,n}^{\text{CG}} =$				
D10		$1/10$	τ	
D100		$1/100$	τ	
D10n		$1/10\ \delta\rho_0\ $	τ	

Table 1: Summary of strategies: the CG tolerances $\tau_{i,n}^{\text{CG}}$ are set as the product of a prefactor (first column) and a common factor shared by all strategies (second column). For the adaptive strategies the third column lists the sections discussing the approximations we make over the prefactor $C_{i,n}$ of Theorem 3.7.

the ℓ_2 error $\|\mathbf{z}_n^{(i)}\|$ of the Sternheimer solution. However, in practical computations we employ both a Schur complement approach [11] as well as kinetic energy preconditioning [51] when solving (3.7). These two approaches modify the effectively employed operator A_n in (3.7) leading to an improvement of the SE conditioning, thus a reduction of the spectral norm $\|A_n^\dagger\|$. In practice making the assumption $\|\mathbf{z}_n^{(i)}\| \approx \|\mathbf{r}_n^{(i)}\|$, i.e. setting $(\epsilon_{N_{\text{occ}}+1} - \epsilon_n) \approx 1$, thus turns out to be a good approximation. This is also demonstrated numerically in Appendix C for our two example systems from Section 4. Motivated by this outcome we keep the terminology “guaranteed” for our **grt** strategy despite making this approximation over Theorem 3.7.

3.3.2. Dropping the Hartree-exchange-correlation kernel term $\|\mathbf{K}\mathbf{v}_i\|$. The Hartree-exchange-correlation kernel is composed of two terms $K^{\text{Hxc}} = K^{\text{H}} + K^{\text{xc}}$. In the absence of spontaneous symmetry breaking the Hartree term usually dominates and the XC term can be neglected (random phase approximation). In a plane-wave basis the Hartree term is a diagonal matrix with entries $(\mathbf{K}_F)_{\mathbf{G},\mathbf{G}} = \frac{4\pi}{\|\mathbf{G}\|^2}$ with the exception $(\mathbf{K}_F)_{\mathbf{00}} = 0$ (due to the compensating background charge). We observe the Coulomb divergence: for small $\|\mathbf{G}\|$ this operator is unbounded. Since the smallest non-zero $\|\mathbf{G}\|$ of the cubic Fourier grid \mathbb{G}^\square is $\frac{2\pi}{\|\mathbf{a}_1\|}$ — with \mathbf{a}_1 denoting the largest cell vector — we obtain that $\|\mathbf{K}_F\| \leq \frac{\|\mathbf{a}_1\|^2}{\pi}$. This leads to the naive bound

$$(3.15) \quad \|\mathbf{K}\mathbf{v}_i\| \simeq \|\mathbf{K}_H\mathbf{v}_i\| \leq \|\mathbf{K}_H\| \|\mathbf{v}_i\| = \|\mathbf{K}_F\| \|\mathbf{v}_i\| \leq \frac{\|\mathbf{a}_1\|^2}{\pi} \|\mathbf{v}_i\|,$$

where in the third step we used that the real-space representation of the Hartree kernel is $\mathbf{K}_H = \mathbf{W}\mathbf{K}_F\mathbf{W}^{-1}$ and that Fourier transforms are unitary. From this development it seems there is little hope that the term $\|\mathbf{K}\mathbf{v}_i\|$ can be dropped: as the system size (thus $\|\mathbf{a}_1\|$) increases it may in principle grow quadratically. This behaviour is indeed observed in practice as Appendix D demonstrates for an aluminium supercell in the absence of preconditioning.

However, when solving the Dyson equation using Kerker-preconditioned GMRES all Krylov vectors in the GMRES subspace as well as the iterates \mathbf{v}_i benefit from the

effect of preconditioning. As the Kerker preconditioner is constructed to counteract the Coulomb divergence the entries of \mathbf{v}_i decay sufficiently rapidly with decreasing $\|\mathbf{G}\|$, such that $\|\mathbf{K}\mathbf{v}_i\|$ stays roughly constant as system size grows, see Appendix D. When modelling insulators Kerker preconditioning is not necessary for $\|\mathbf{K}_H\mathbf{v}_i\|$ to remain constant as the Coulomb divergence is in this case compensated by the large-wavelength limit of χ_0 [30, 14]. Overall employing appropriate preconditioning of the Dyson equation the term $\|\mathbf{K}\mathbf{v}_i\|$ thus stays small even for large systems motivating us to drop this term for our **bal** and **agr** strategies.

3.3.3. Replacing the orbital term by its lower bound. For the orbital term $\|\text{Re}(\mathbf{F}^{-1}\Phi)\|_{2,\infty}$ we can derive upper and lower bounds.

PROPOSITION 3.10. *With the notations defined above, we have*

$$(3.16) \quad \sqrt{\frac{N_{\text{occ}}}{|\Omega|}} \leq \|\mathbf{F}^{-1}\Phi\|_{2,\infty} \leq \sqrt{\frac{N_g}{|\Omega|}}.$$

Proof. It suffices to prove $\sqrt{\frac{N_{\text{occ}}}{N_g}} \leq \|\Phi_{\text{real}}\| \leq 1$ where $\Phi_{\text{real}} = \sqrt{\frac{|\Omega|}{N_g}} \mathbf{F}^{-1}\Phi$. By the definition of \mathbf{F}^{-1} (2.21) and the fact that Φ has orthonormal columns, Φ_{real} also has orthonormal columns. Therefore, for the upper bound, it follows from $\|\Phi_{\text{real}}(i, :)\| \leq \|\Phi_{\text{real}}\| = 1$ for $i = 1, \dots, N_g$. For the lower bound, it follows from

$$(3.17) \quad N_{\text{occ}} = \sum_{j=1}^{N_{\text{occ}}} \|\Phi_{\text{real}}(:, j)\|^2 = \sum_{i=1}^{N_g} \|\Phi_{\text{real}}(i, :)\|^2 \leq N_g \max_{i=1, \dots, N_g} \|\Phi_{\text{real}}(i, :)\|^2. \quad \square$$

The upper bound is not useful since it is very pessimistic, essentially assuming localisation of the orbitals at a single grid point. This contrasts with the typical behavior of orbitals in practical Kohn-Sham DFT calculations, where the (pseudopotential) model is precisely chosen to achieve a smooth real-space functional form, resulting in fast Fourier decay. For this reason we will replace the orbital term by its lower bound in our **bal** and **agr** strategies. However, if this approximation was not satisfactory we could keep the term $\|\text{Re}(\mathbf{F}^{-1}\Phi)\|_{2,\infty}$ as its computation is a cheap one-time cost.

Remark 3.11 (Scaling of the bounds with system size). While it is in general easy to construct practical heuristics for convergence tolerances which work well in small material systems, it is much harder to make sure these heuristics keep working for larger, more realistic systems. To ensure our strategies (see Table 1) do not deteriorate for larger systems, we will explicitly analyse their scaling with system size. Consider extending the simulation cell by building a supercell made up of ℓ replica in one Cartesian direction. In this process both the cell volume $|\Omega|$ and the number of electrons N_{occ} scale linearly with ℓ . The approximate scaling of N_g in equation (2.17) establishes an approximate linear scaling of N_g with ℓ as well. Consider the exact prefactor of Theorem 3.7

$$C_{i,n} = \frac{\epsilon_{N_{\text{occ}}+1} - \epsilon_n}{\|\mathbf{K}\mathbf{v}_i\| \|\text{Re}(\mathbf{F}^{-1}\Phi)\|_{2,\infty}} \frac{\sqrt{|\Omega|}}{2f_n \sqrt{N_g N_{\text{occ}}}}.$$

Since both the upper and lower bound of $\|\text{Re}(\mathbf{F}^{-1}\Phi)\|_{2,\infty}$ obtained in Proposition 3.10 do not scale with ℓ we can deduce this term to be asymptotically invariant to ℓ as well. Following our arguments in Sections 3.3.1 and 3.3.2 an appropriate preconditioning of the CG as well as Dyson equations should keep the eigenvalue difference as well as the kernel term invariant to ℓ . Overall we expect $C_{i,n} = O(1/\sqrt{\ell})$.

By similar arguments we can deduce this scaling with ℓ to be conserved for our proposed **grt** and **bal** strategies, but violated for **agr**. When solving the Dyson equation using the **agr** strategy we would thus expect the final true GMRES residual to deviate from the desired tolerance τ more and more as ℓ gets larger. This trend is indeed observed in our numerical experiments (see Table 6).

4. Numerical experiments.

4.1. From theory to computation: methodology and general setup.

4.1.1. Modelling perfect crystals. In our numerical experiments we will target problems from condensed matter physics to demonstrate the efficiency and accuracy of our adaptive CG tolerance strategies. In condensed matter simulations materials are commonly modelled as perfect crystals, i.e. systems in which a finite-sized simulation cell (the unit cell Ω) is infinitely repeated periodically, forming a Bravais lattice \mathbb{L} . To avoid dealing with an infinitely large problem, practical simulations commonly employ the *supercell* approach, in which the unit cell Ω is only repeated finite times in each direction. For example, a $\ell_1 \times \ell_2 \times \ell_3$ supercell is formed by repeating Ω respectively ℓ_1 , ℓ_2 , and ℓ_3 times in the directions of the lattice vectors, thus leading to a system consisting of $L = \ell_1 \ell_2 \ell_3$ unit cells. At the boundary one employs periodic boundary conditions to avoid artificial surface effects.

When solving the Kohn-Sham problem on a $\ell_1 \times \ell_2 \times \ell_3$ supercell we are thus in the setting of Section 2 with respectively a larger simulation cell. This will lead to a L -times larger eigenvalue problem with L -times more occupied orbitals to be computed (since $N_b, N_{\text{occ}} \sim L|\Omega|$ as discussed in Remark 3.11). When treated naively this would drive up computational cost by a factor L^3 . However, assuming no spontaneous symmetry breaking the KS ground state keeps the \mathbb{L} -translational invariance of the Hamiltonian even when performing the simulation in a supercell. As a result Bloch theory enables to relabel the supercell orbitals ϕ_n as $\phi_{n\mathbf{k}}(\mathbf{r}) = e^{i\mathbf{k}\cdot\mathbf{r}} u_{n\mathbf{k}}(\mathbf{r})$, where we re-indexed n as (n, \mathbf{k}) . See e.g. [47, Section XIII.16] for more details. Notably $u_{n\mathbf{k}}$ is again \mathbb{L} -periodic and the Kohn-Sham equations (2.3) can be rewritten as $H_{\rho,\mathbf{k}} u_{n\mathbf{k}} = \epsilon_{n\mathbf{k}} u_{n\mathbf{k}}$ with increasing eigenvalues $\epsilon_{n\mathbf{k}}$, orthonormal eigenfunctions $u_{n\mathbf{k}}$ and the \mathbf{k} -point Hamiltonian $H_{\rho,\mathbf{k}} = \frac{1}{2}(-i\Delta + \mathbf{k})^2 + V_{\text{ext}}(\mathbf{r}) + V_{\rho}^{\text{Hxc}}(\mathbf{r})$ (c.f. (2.4)). The electronic density ρ is rewritten as (c.f. (2.5))

$$\rho(\mathbf{r}) = \frac{1}{L} \sum_{\mathbf{k} \in \mathcal{G}_{\text{MP}}} \sum_{n=1}^{\infty} f_{n\mathbf{k}} |u_{n\mathbf{k}}(\mathbf{r})|^2, \quad f_{n\mathbf{k}} = f_{\text{FD}} \left(\frac{\epsilon_{n\mathbf{k}} - \epsilon_{\text{F}}}{T} \right), \quad \frac{1}{L} \sum_{\mathbf{k} \in \Omega^*} \sum_{n=1}^{\infty} f_{n\mathbf{k}} = N. \quad (4.1)$$

Here, Ω^* is the first Brillouin zone, the unit cell of the dual lattice \mathbb{L}^* of \mathbb{L} . Moreover the grid $\mathcal{G}_{\text{MP}} = \Omega^* \cap \left(\mathbb{Z} \frac{\mathbf{b}_1}{\ell_1} + \mathbb{Z} \frac{\mathbf{b}_2}{\ell_2} + \mathbb{Z} \frac{\mathbf{b}_3}{\ell_3} \right)$ is known as the Monkhorst-Pack grid [44] in the physics literature. One can show that in the thermodynamic limit $L \rightarrow \infty$ these equations approach the solution of the Kohn-Sham problem for perfect crystals. In this limit the sums over \mathbf{k} in (4.1) become integrals over the Brillouin zone Ω^* . An equivalent interpretation of the supercell method is thus as a quadrature of such integrals over Ω^* with quadrature nodes \mathcal{G}_{MP} .

This supercell approach thus reduces the complexity massively as only computations on the unit cell need to be performed. Moreover each \mathbf{k} -point-specific Hamiltonian can be treated independently leading to a natural parallelism, which can be easily exploited during the computation. For more details on the supercell approach see [41, Section 2.8], for a proof of the thermodynamic limit in the setting of reduced Hartree-Fock theory, see [8, 16, 23] and for an analysis of common Brillouin zone

quadrature schemes see [9].

Following a similar argument one can employ Bloch theory to obtain a representation of the application $\chi_0 \delta V$ in terms of Bloch modes. Comparing to (2.10) this amounts to adding an additional sum over \mathbf{k} -points, i.e.

$$(4.2) \quad \chi_0 \delta V = \frac{1}{L} \sum_{\mathbf{k} \in \mathcal{G}_{\text{MP}}} \sum_{n=1}^{N_{\text{occ},\mathbf{k}}} 2f_{n\mathbf{k}} \text{Re}(\phi_{n\mathbf{k}}^* \delta \phi_{n\mathbf{k}}) + \delta f_{n\mathbf{k}} |\phi_{n\mathbf{k}}|^2,$$

where we understand $\phi_{n\mathbf{k}}(\mathbf{r}) = e^{i\mathbf{k} \cdot \mathbf{r}} u_{n\mathbf{k}}(\mathbf{r})$. In this work we only consider lattice-periodic perturbations δV , such that the orbital responses $\delta \phi_{n\mathbf{k}} = \delta \phi_{n\mathbf{k}}^P + \delta \phi_{n\mathbf{k}}^Q$ have identical structure to the expressions in Section 2, the main change being an additional index \mathbf{k} , namely

$$(4.3) \quad \delta \phi_{n\mathbf{k}}^P = \sum_{m=1}^{N_{\text{occ},\mathbf{k}}} \frac{f_{n\mathbf{k}}^2}{f_{n\mathbf{k}}^2 + f_{m\mathbf{k}}^2} \frac{f_{n\mathbf{k}} - f_{m\mathbf{k}}}{\epsilon_{n\mathbf{k}} - \epsilon_{m\mathbf{k}}} \langle \phi_{m\mathbf{k}}, \delta V \phi_{n\mathbf{k}} \rangle \phi_{m\mathbf{k}}$$

for $n = 1, \dots, N_{\text{occ},\mathbf{k}}$ and $\mathbf{k} \in \mathcal{G}_{\text{MP}}$. $\phi_{n\mathbf{k}}^Q$ is again obtained by solving a Sternheimer equation $Q(H_{\rho,\mathbf{k}} - \epsilon_{n\mathbf{k}})Q\delta\phi_{n\mathbf{k}}^Q = -Q(\delta V \phi_{n\mathbf{k}})$. Therefore, Theorem 3.7 and the adaptive strategies proposed in Section 3.3 remain applicable due to the similar mathematical structure. The main change is to replace n in the prefactor $C_{i,n}$ by $n\mathbf{k}$ and note that the number of occupied orbitals N_{occ} is now the sum of the number of occupied orbitals for each \mathbf{k} -point, i.e. $N_{\text{occ}} = \sum_{\mathbf{k}} N_{\text{occ},\mathbf{k}}$.

4.1.2. Implementation and computational setup. We implemented the inexact GMRES framework (Algorithm 3.1) within the Density-Functional ToolKit (DFTK) [33] — an accessible framework for mathematical research on plane-wave DFT methods written in the Julia programming language [5]. Unless otherwise specified we followed previous work [11] on DFPT problems and employed a uniform Monkhorst-Pack grid to discretise the Brillouin zone, the PBE exchange-correlation functional [46] and GTH pseudopotentials [22, 29]. Our DFPT test problems are obtained by solving the self-consistent field problem without any perturbation, followed by introducing a perturbing potential $\delta \mathbf{V}_0$ resulting from displacing the atomic positions in the simulation cell. This perturbation provides the right-hand side $\chi_0 \delta \mathbf{V}_0$ of a Dyson equation (2.24), which is solved using Algorithm 3.1. Throughout our experiments we employ a zero initial guess ($\mathbf{x}_0 = \mathbf{0}$) and use an initial estimate $s = 1$ for $\sigma_m(\mathbf{H}_m)$. For the inexact applications of the dielectric operator we solve the Sternheimer equations using the Schur complement trick of [11] as well as a CG solver with kinetic energy preconditioning (the kinetic operator is the scaled inverse Laplacian, which is diagonal in a Fourier representation). The employed CG convergence tolerances $\tau_{i,n\mathbf{k}}^{\text{CG}}$ are chosen adaptively according to one of the adaptive strategies from Table 1. For each Sternheimer solve a minimum of one CG iteration is performed even if the initial residual norm is already below this tolerance.

The full source code to reproduce the experiments, along with more exhaustive numerical tests, is available at https://github.com/bonans/inexact_Krylov_response. The adaptive algorithm introduced in this work is planned to become the default Dyson equation solver in an upcoming version of DFTK.

4.1.3. Performance metrics. In our experiments we will employ the following three metrics to compare our various strategies:

Cost. The cost for solving the Dyson equation is dominated by the cost of solving the N_{occ} Sternheimer equations for each GMRES iteration. In turn the cost of solving a Sternheimer equation is directly related to the number of applications of the Hamiltonian \mathbf{H}_ρ as its most expensive step. We thus employ the total number of Hamiltonian applications N^{Ham} as a measure to evaluate the computational cost.

Accuracy. Some strategies for adaptively selecting the CG tolerances violate theorem 3.7, such that accuracy of the solutions \mathbf{x}_{end} returned by the inexact GMRES can vary. We compare accuracies by making reference to the *true* residual norm $\|\mathbf{r}_{\text{end}}\| = \|\mathbf{b} - \mathcal{E}\mathbf{x}_{\text{end}}\|$, which is obtained by applying the dielectric adjoint \mathcal{E} with the CG tolerance of all Sternheimer equations tightened to 10^{-16} . Similarly when discussing the residuals at the i -th GMRES iteration we make the distinction between the *estimated* residual $\|\tilde{\mathbf{r}}_i\|$, which is employed in the GMRES procedure itself, and the *true* residuals $\|\mathbf{r}_i\| = \|\mathbf{b} - \mathcal{E}\mathbf{x}_i\|$, obtained by an explicit re-computation using tight Sternheimer tolerances.

Efficiency. Different strategies for selecting the CG tolerances show an intrinsic trade-off between the computational cost and obtained accuracy. To quantify this balance more systematically we introduce the (absolute) efficiency

$$(4.4) \quad \eta := -\frac{\log_{10}(\|\mathbf{r}_{\text{end}}\|/\|\mathbf{r}_0\|)}{N^{\text{Ham}}} > 0,$$

where $\|\mathbf{r}_0\|$ ($\|\mathbf{r}_{\text{end}}\|$) is the initial (final) true residual. Note that η effectively measures the average residual reduction per Hamiltonian application and can also be interpreted as the convergence rate in terms of the number of Hamiltonian applications. Additionally, we use a *relative efficiency* η_{rel} — that is the ratio of η of one strategy with respect to a reference. For example, $\eta_{\text{rel}} = 2$ indicates that compared to the reference half as many Hamiltonian applications are needed to achieve the same accuracy.

4.2. Systematic comparison of strategies on an aluminium supercell.

We first compare our various strategies for setting the CG tolerances (Table 1), both with and without preconditioning in the outer inexact GMRES. As an example we take a standard problem in condensed matter physics, namely an elongated metallic supercell. Specifically we take an aluminium supercell with 40 atoms obtained by repeating a 4-atom cubic unit cell 10 times in the x direction, see Figure 3 (A). On top of the parameters of section 4.1.2 we chose $E_{\text{cut}} = 40$ Ha, Fermi-Dirac smearing with temperature $T = 10^{-3}$ Ha and a $1 \times 3 \times 3$ \mathbf{k} -point grid. In this setup the Dyson equation has size $N_g = 911\,250$ and each application of the dielectric adjoint \mathcal{E} requires solving $N_{\text{occ}} = 569$ SEs, each of size $N_b \approx 54\,200$. We remark that in standard computational setups approximations are more consistent across \mathbf{k} -points if one constructs the spherical Fourier basis in (2.16) by the condition $\|\mathbf{G} + \mathbf{k}\|_2 \leq \sqrt{2E_{\text{cut}}}$ — thus making the basis and thus N_b differ across \mathbf{k} points [10].

In Table 2 we summarise the performance metrics of various strategies for $\tau = 10^{-9}$ and a GMRES restart size $m = 20$. The CG tolerances $\tau_{i,n\mathbf{k}}^{\text{CG}}$ are set according to Table 1 and the relative efficiency η_{rel} is given against the D10 strategy. When employing a Kerker preconditioner (Remark 3.9) in the inexact GMRES we prefix the corresponding strategy by a P. For instance, **Pgrt** refers to employing both the Kerker preconditioner as well as the **grt** strategy for selecting CG tolerances. Note that for **grt** and **D10n** we only tested the preconditioned versions as the non-preconditioned versions are too computationally expensive without offering additional insights.

We observe our adaptive strategies (highlighted in blue) to consistently yield

Strategy	agr	bal	D10	D100	Pagr	Pbal	Pgrt	PD10	PD100	PD10n
$\ \mathbf{r}_{\text{end}}\ $	2e-7	6e-9	9e-6	7e-7	2e-8	7e-10	2e-10	1e-5	1e-6	5e-9
N^{Ham}	385 k	453 k	499 k	539 k	168 k	196 k	228 k	194 k	219 k	275 k
η_{rel}	1.53	1.50	1.00	1.04	3.87	3.71	3.31	2.52	2.49	2.47

Table 2: **Aluminium supercell:** Accuracy of the returned solution $\|\mathbf{r}_{\text{end}}\|$, total number of Hamiltonian applications N^{Ham} and relative efficiency η_{rel} (referencing D10) for the aluminium supercell with $\tau = 10^{-9}$. Adaptive strategies are highlighted in blue, and the top three strategies for each metric are highlighted in orange.

higher final accuracy while requiring similar or fewer Hamiltonian applications compared to baseline strategies. For example, switching from a naive D10 or D100 to our **bal** strategy speeds up the computation by a factor 1.5 as illustrated by the relative efficiency row. By large this is due the ability of our adaptive strategies to linearly reduce the number of CG iterations to solve the SEs across the GMRES iterations — until just 1 or 2 CG iterations are needed in the final GMRES steps. See Appendix E for a numerical demonstration of this behaviour. When combining adaptive CG tolerances with GMRES preconditioning, this effect augments to saving almost a factor of 4 compared to D10. This illustrates Kerker preconditioning to bring noteworthy efficiency gains for metallic systems, in agreement with Remark 3.9. With respect to the accuracy we observe that only the preconditioned adaptive strategies **Pgrt** and **Pbal** achieve a true residual norm below the desired tolerance $\tau = 10^{-9}$, while the non-preconditioned **bal** fails in doing so — again emphasising the need for appropriate preconditioning when dropping the Hartree-exchange-correlation kernel term $\|\mathbf{K}\mathbf{v}_i\|$ from our estimates (Section 3.3.2). Furthermore we notice the failure of all **agr** and baseline variants to achieve the prescribed tolerance. Overall **Pbal** stays in the top 3 (highlighted in orange) for all metrics and achieves the desired tolerance in only insignificantly more Hamiltonian applications compared to PD10 — thus representing the best compromise in this example.

This impression of our proposed adaptive CG tolerance strategies is confirmed when considering Figures 3 (A) and (B), displaying the convergence of the true residuals of the GMRES method versus the GMRES iteration number i and the accumulated number of Hamiltonian applications. In particular for our strategies (solid lines) Figure 3 (A) shows that the convergence rate of the outer GMRES iterations is not significantly affected by using inexact matrix-vector products $\mathcal{E}\mathbf{v}$ until the final stages of the iterations. Most notably the **Pbal** and **Pgrt** strategies (i.e. employing appropriate preconditioning) keep a steady linear convergence wrt. i until the desired tolerance τ has been reached. Finally Figure 3 (B) confirms the superlinear convergence of our adaptive strategies with respect to the number of Hamiltonian applications and thus the accumulated computational cost — as expected from Remark 3.8. Again **Pbal** and **Pgrt** emerge as the best compromises between accuracy and cost.

We remark that the trends and overall conclusions of this experiment are stable with respect to target accuracy τ , Krylov size m or the size of the aluminium system as a more exhaustive study presented in Appendix F illustrates.

4.3. Targeting a complex material: Heusler alloy. We consider the Fe_2MnAl transition-metal alloy as an example for a condensed matter system with a considerably more challenging electronic structure than aluminium. It is an example of a Heusler alloy, a class of materials, which are of practical interest due to their

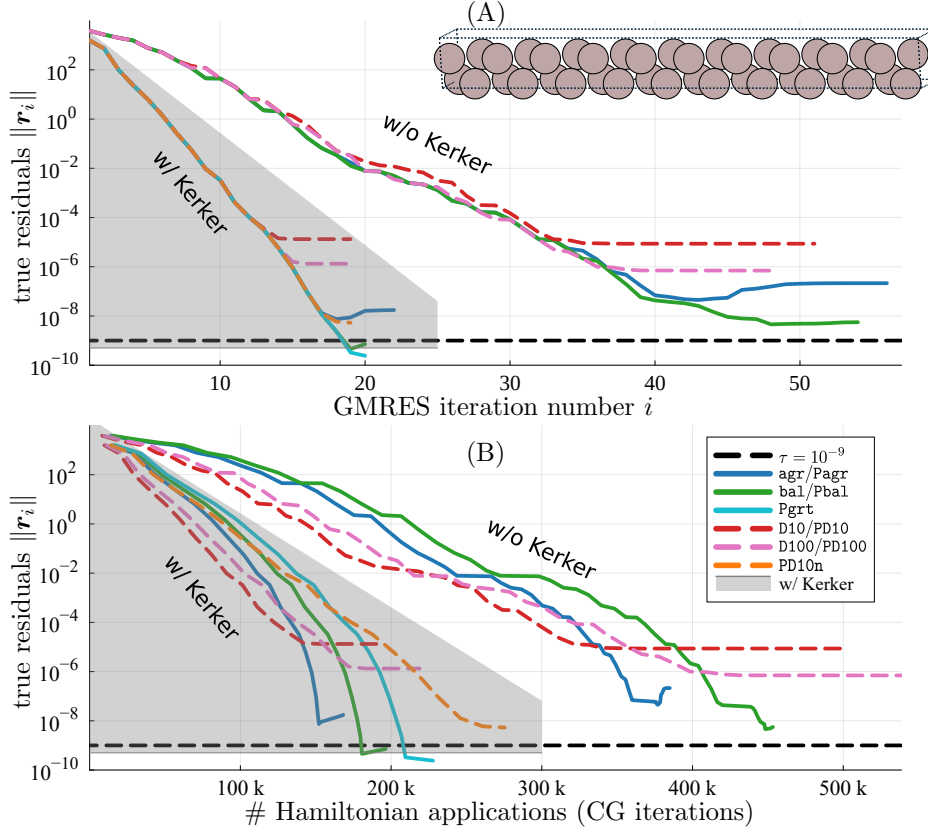


Fig. 3: **Aluminium supercell**: True residual norms $\|r_i\|$ v.s. (A) number of GMRES iterations, (B) accumulated number of Hamiltonian applications. The shaded areas indicate the strategies with Kerker preconditioning.

rich and unusual magnetic and electronic properties. For example, Fe_2MnAl is a half-metal, which loosely speaking means that depending on the spin degree of freedom the material behaves either like a metal or like an insulator. This behaviour is quite susceptible to the external conditions, such that the electronic density of the material can change drastically under a small perturbing potential δV_0 . Numerically this makes the Dyson equation is more challenging to solve. See [30] and reference therein for more details as well as an analysis of the SCF convergence on such systems.

For modelling the Fe_2MnAl alloy we employ the parameters of Section 4.1.2 as well as $E_{\text{cut}} = 45$ Ha, Gaussian smearing with temperature $T = 10^{-2}$ Ha and a $13 \times 13 \times 13$ \mathbf{k} -point grid. This results in $N_g = 250\,000$, $N_{\text{occ}} = 24\,612$ and $N_b \approx 4\,820$. For the inexact GMRES we employ a restart size of $m = 10$ as well as a Kerker preconditioner in order to capture the Coulomb divergence in the metallic channel of this material.

We solve the Dyson equation until a tolerance of $\tau = 10^{-9}$ using a selection of strategies for selecting the CG tolerance, see Table 3 and Figure 4. Comparing to the aluminium system the problem sizes of the Dyson and Sternheimer equations (N_g and N_b) are much smaller. Still, the difficulty of this system is clearly visible from the total number of Hamiltonian applications required to reach convergence as well as the inability of the baseline strategies PD10 and PD100 to obtain accurate solutions — with

Strategy	agr	bal	D10	D100	Pagr	Pbal	Pgrt	PD10	PD100	PD10n
$\ \mathbf{r}_{\text{end}}\ $	3e-8	4e-9	2e-6	1e-7	1e-8	8e-10	3e-10	2e-6	1e-7	1e-9
N^{Ham}	12 M	15 M	21 M	22 M	10 M	12 M	15 M	16 M	16 M	20 M
η_{rel}	2.06	1.85	1.00	1.09	2.54	2.33	1.96	1.33	1.47	1.42

Table 3: **Heusler:** Accuracy of the returned solution $\|\mathbf{r}_{\text{end}}\|$, total number of Hamiltonian applications N^{Ham} and relative efficiency η_{rel} (referencing D10) for the Heusler system with $\tau = 10^{-9}$. Adaptive strategies are highlighted in blue, and the top three strategies for each metric are highlighted in orange.

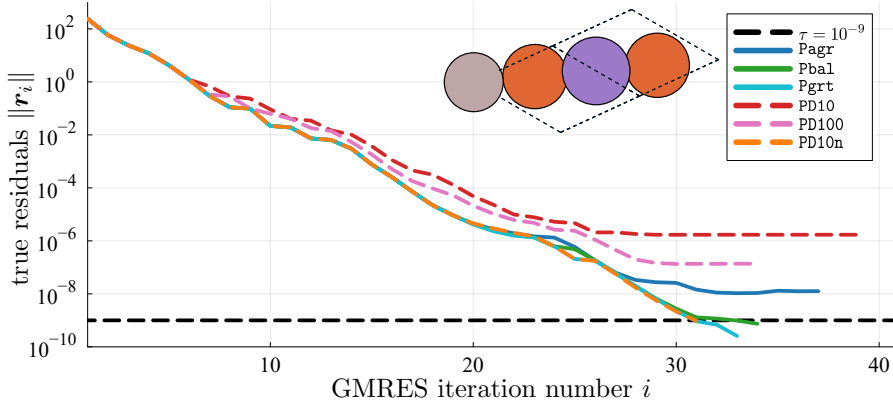


Fig. 4: **Heusler:** True residual norm $\|\mathbf{r}_i\|$ vs. GMRES iteration i for the Fe_2MnAl Heusler system. The inset shows the structure of Fe_2MnAl with iron (Fe) in orange, manganese (Mn) in violet and aluminium (Al) in grey.

final true residuals being two orders larger than the requested accuracy τ . For these two baseline strategies we also notice an early deviation from ideal convergence in Figure 4. In contrast our adaptive strategies **Pbal** and **Pgrt** stay close to the baseline **PD10n** accuracy and keep a steady linear convergence. We further remark that also for this Heusler system we observe a superlinear convergence in the total number of Hamiltonian applications for adaptive strategies similar to Figure 3 (B).

For this system our **Pbal** strategy again provides the best compromise. It achieves both the desired accuracy of $\tau = 10^{-9}$ while at the same time requiring about 40% Hamiltonian applications less compared to the equally accurate **PD10n** baseline strategy — in absolute numbers a saving of about 8 million Hamiltonian applications. This demonstrates our adaptive CG tolerance strategies to be reliably applicable also for challenging material systems.

4.4. Semiconductors: Silicon. We consider a simple silicon primitive unit cell with two silicon atoms to demonstrate our adaptive CG tolerance strategies to be applicable to semiconductors and insulators. For the silicon systems we consider a $8 \times 8 \times 8$ \mathbf{k} -point grid with $E_{\text{cut}} = 40$ Ha and no smearing. This results in $N_g = 91\,125$, $N_{\text{occ}} = 2\,048$ and $N_b \approx 3\,020$. In the context of SCF methods it is well known that for a semiconducting material a Kerker preconditioner should not be employed to obtain best convergence, see e.g. the discussion in [30]. In line with Remark 3.9 we thus also refrain from preconditioning the inexact GMRES for silicon. For a

Strategy	agr	bal	grt	D10	D100	D10n
$\ \mathbf{r}_{\text{end}}\ $	8e-10	3e-10	2e-10	3e-8	3e-9	2e-10
N^{Ham}	263 k	301 k	300 k	340 k	379 k	436 k
η_{rel}	1.49	1.37	1.37	1.00	0.99	0.95

Table 4: **Silicon:** Accuracy of the returned solution $\|\mathbf{r}_{\text{end}}\|$, total number of Hamiltonian applications N^{Ham} and relative efficiency η_{rel} (referencing D10) for silicon with $\tau = 10^{-9}$. Adaptive strategies are highlighted in blue, and the top three strategies for each metric are highlighted in orange.

GMRES convergence tolerance $\tau = 10^{-9}$ this results in the performance metrics of Table 4, whereas consistently worse results are obtained with Kerker preconditioning. In agreement with the metallic systems our adaptive strategies turn out to be reliable, all achieving a better accuracy than the prescribed tolerance $\tau = 10^{-9}$. While **agr** and **grt** turn out to be slightly less costly for this simple material, **bal** still remains a good compromise saving about 30% compared to D10n— as the only baseline strategy also achieving the accuracy τ .

5. Conclusions. The efficient simulation of linear response properties in density functional theory requires the iterative solution of the Dyson equation. This is a nested linear problem, in which each application of the operator in turn requires solving a sizeable number of Sternheimer equations (SE) iteratively. In this work, we have performed an error analysis for the numerical solution of the Dyson equation in plane-wave basis sets, quantifying rigorously the error propagation from the approximate SE solutions to the final Dyson solution. Based on this analysis and several physically motivated modifications, we have proposed a set of strategies for adaptively selecting the convergence tolerance $\tau_{i,n}^{\text{CG}}$ when solving the SEs. When employing an inexact GMRES framework to solve the Dyson equation this allowed us to robustly tune the tightness of SE solution in each iteration of the outer GMRES solver. In non-trivial test cases on practically relevant materials systems this enabled our recommended **bal** (balanced) strategy to obtain a reduction of computational time by about 40% while maintaining the accuracy. This is in contrast to baseline strategies, which feature a heuristically tuned constant SE tolerance and which we could demonstrate to frequently fail to achieve a sufficiently accurate solution. Our framework combines well with common preconditioning strategies in the field. For example in combination with the Kerker preconditioner (commonly employed in self-consistent field methods) we could obtain an additional 20% reduction of the cost for solving the Dyson equation in metallic systems.

Overall this work presents a first approach for solving the Dyson equation employing exclusively Krylov subspace methods. Making use of the inexact Krylov subspace formalism our work offers a reliable and efficient black-box solver for DFPT without the need for any heuristic tuning of tolerances. With the obtained efficiency gains our strategies thus provide a viable alternative to the more wide-spread approaches based on accelerated fixed-point methods [24, 3, 26] in the field. However, in contrast to the latter Krylov-subspace methods are mathematically well-studied, such that there are several promising directions to extend the foundations of this work. First, when requiring only a low-accuracy SE solution one could employ lower-precision arithmetics to provide further speedups on modern GPU-based compute architectures. Second, since the SEs form a sequence of closely related linear systems, Krylov sub-

space recycling techniques could be explored. Finally, our framework can be easily extended to the perturbation theory of other mean-field models, such as Hartree-Fock or Gross-Pitaevskii equations, where the Dyson equation is replaced by an alternative linearization of the underlying nonlinear eigenvalue problem.

Appendix A. Proof of inexact GMRES lemmas in Section 3.2.

Proof of Lemma 3.1. By the inexact Arnoldi decomposition (3.2) and the definition of $\mathbf{E}_i = \tilde{\mathcal{E}}^{(i)} - \mathcal{E}$, we have

$$(A.1) \quad \mathcal{E} \mathbf{V}_m + [\mathbf{E}_1 \mathbf{v}_1, \mathbf{E}_2 \mathbf{v}_2, \dots, \mathbf{E}_m \mathbf{v}_m] = \mathbf{V}_{m+1} \mathbf{H}_m.$$

Therefore, we can write the true residual \mathbf{r}_m as

$$(A.2) \quad \begin{aligned} \mathbf{r}_m &= \mathbf{b} - \mathcal{E} \mathbf{x}_m = \mathbf{b} - \mathcal{E} \mathbf{x}_0 - \mathcal{E} \mathbf{V}_m \mathbf{y}_m \\ &= \mathbf{b} - \mathcal{E} \mathbf{x}_0 - \mathbf{V}_{m+1} \mathbf{H}_m \mathbf{y}_m + [\mathbf{E}_1 \mathbf{v}_1, \mathbf{E}_2 \mathbf{v}_2, \dots, \mathbf{E}_m \mathbf{v}_m] \mathbf{y}_m \\ &= \mathbf{E}_0 \mathbf{x}_0 + \mathbf{V}_{m+1} (\beta \mathbf{e}_1 - \mathbf{H}_m \mathbf{y}_m) + [\mathbf{E}_1 \mathbf{v}_1, \mathbf{E}_2 \mathbf{v}_2, \dots, \mathbf{E}_m \mathbf{v}_m] \mathbf{y}_m, \end{aligned}$$

where for the last equality, we used the fact that $\mathbf{V}_{m+1} \mathbf{e}_1 = \mathbf{v}_1 = \mathbf{r}_0 / \beta$ and $\mathbf{r}_0 = \mathbf{b} - \tilde{\mathcal{E}}^{(0)} \mathbf{x}_0$ due to the Arnoldi process. The result then follows from the definition of estimated residual $\tilde{\mathbf{r}}_m = \beta \mathbf{e}_1 - \mathbf{H}_m \mathbf{y}_m$, the orthonormality of \mathbf{V}_{m+1} , and the triangle inequality. \square

Proof of Lemma 3.2. We give a simpler proof of this result compared to the one provided in [50]. Note that

$$(A.3) \quad \begin{aligned} [\mathbf{y}_m]_i &= \mathbf{e}_i^* \mathbf{y}_m = \mathbf{e}_i^* \mathbf{H}_m^\dagger \beta \mathbf{e}_1 = \mathbf{e}_i^* \mathbf{H}_m^\dagger \beta \mathbf{e}_1 - \mathbf{e}_i^* \mathbf{H}_m^\dagger \begin{bmatrix} \mathbf{H}_{i-1} \mathbf{y}_{i-1} \\ \mathbf{0} \end{bmatrix} \\ &= \mathbf{e}_i^* \mathbf{H}_m^\dagger \begin{bmatrix} \beta \mathbf{e}_1 - \mathbf{H}_{i-1} \mathbf{y}_{i-1} \\ \mathbf{0} \end{bmatrix} = \mathbf{e}_i^* \mathbf{H}_m^\dagger \begin{bmatrix} \tilde{\mathbf{r}}_{i-1} \\ \mathbf{0} \end{bmatrix}, \end{aligned}$$

where \mathbf{H}_m^\dagger is the pseudoinverse of \mathbf{H}_m . Therefore

$$(A.4) \quad |[\mathbf{y}_m]_i| \leq \|\mathbf{e}_i^* \mathbf{H}_m^\dagger\| \|\tilde{\mathbf{r}}_{i-1}\| \leq \frac{1}{\sigma_m(\mathbf{H}_m)} \|\tilde{\mathbf{r}}_{i-1}\|. \quad \square$$

Appendix B. Kerker preconditioner. Denoting the discrete Fourier transform matrix by $\mathbf{W} \in \mathbb{C}^{N_g \times N_g}$ (see (2.21)) the discretised Kerker preconditioner is $\tilde{\mathbf{T}} = \mathbf{W}^{-1} \mathbf{D} \mathbf{W}$, where $\mathbf{D} \in \mathbb{C}^{N_g \times N_g}$ — its representation in Fourier space — is the diagonal matrix with entries

$$(B.1) \quad \frac{\|\mathbf{G}\|^2}{\|\mathbf{G}\|^2 + \alpha^2}, \quad \mathbf{G} \in \mathbb{G}^\square$$

and $\alpha > 0$ is an appropriately chosen parameter. In practice, to ensure that applying the Kerker preconditioner conserves the total charge one employs the modification

$$(B.2) \quad \mathbf{T} = \left(\mathbf{1}_{N_g} - \frac{1}{N_g} \mathbf{1}_{N_g} \mathbf{1}_{N_g}^\top \right) \mathbf{W}^{-1} \mathbf{D} \mathbf{W} + \frac{1}{N_g} \mathbf{1}_{N_g} \mathbf{1}_{N_g}^\top,$$

where $\mathbf{1}_{N_g} \in \mathbb{C}^{N_g}$ is the vector of all ones. Note that due to the definition of the discrete Fourier transform matrix

$$(B.3) \quad \mathbf{1}_{N_g}^\top \mathbf{W}^{-1} = \sqrt{N_g} \mathbf{e}_1^\top, \quad \mathbf{e}_1^\top \mathbf{W} = \frac{1}{\sqrt{N_g}} \mathbf{1}_{N_g}^\top, \quad \mathbf{W}^{-1} \mathbf{e}_1 = \frac{1}{\sqrt{N_g}} \mathbf{1}_{N_g}.$$

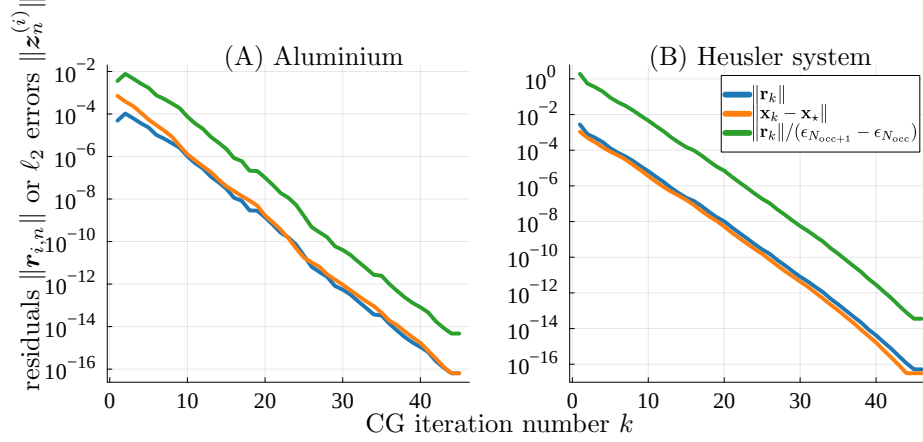


Fig. 5: Residual norms $\|\mathbf{r}_n^{(i)}\|$, ℓ_2 errors $\|\mathbf{z}_n^{(i)}\|$ and error bounds $\|\mathbf{r}_n^{(i)}\|/(\epsilon_{N_{\text{occ}}+1} - \epsilon_{N_{\text{occ}}})$ v.s. CG iteration number k for the worst conditioned Sternheimer equation of (A) the Aluminium system with $\ell = 10$ and (B) the Heusler system described in Section 4.

we have

$$(B.4) \quad \mathbf{1}_{N_g} \mathbf{1}_{N_g}^\top \mathbf{W}^{-1} \mathbf{D} \mathbf{W} = \sqrt{N_g} \mathbf{1}_{N_g} \mathbf{e}_1^\top \mathbf{D} \mathbf{W} = \sqrt{N_g} D_{11} \mathbf{1}_{N_g} \mathbf{e}_1^\top \mathbf{W} = D_{11} \mathbf{1}_{N_g} \mathbf{1}_{N_g}^\top,$$

where D_{11} is the first diagonal entry of \mathbf{D} . Therefore inserting (B.4) into (B.2) one shows

$$(B.5) \quad \mathbf{T} = \mathbf{W}^{-1} \mathbf{D} \mathbf{W} - \frac{D_{11}}{\sqrt{N_g}} \mathbf{1}_{N_g} \mathbf{1}_{N_g}^\top + \frac{1}{\sqrt{N_g}} \mathbf{1}_{N_g} \mathbf{1}_{N_g}^\top = \mathbf{W}^{-1} (\mathbf{D} + (1 - D_{11}) \mathbf{e}_1 \mathbf{e}_1^\top) \mathbf{W}.$$

Equation (B.2) is thus equivalent to setting the first diagonal entry of \mathbf{D} to be 1. A consequence of this and the properties of the unitarity of the Fourier transform is:

LEMMA B.1. *The Kerker preconditioner \mathbf{T} is a Hermitian positive definite matrix with the maximum eigenvalue $\lambda_{\max} = 1$, in particular $\|\mathbf{T}\| = 1$.*

Appendix C. Bound prefactor without eigenvalue gaps. In Section 3.3.1 of the main text we argue that the eigenvalue gap term $(\epsilon_{N_{\text{occ}}+1} - \epsilon_n)$ in the prefactor $C_{i,n}$ of Theorem 3.7 can be discarded, i.e. set to 1 in practical calculations provided that appropriate techniques such as preconditioning or the Schur complement approach [11] are employed. Indeed, this can be demonstrated numerically, see

Figure 5. In this plot we show the ℓ_2 norm of the CG error $\mathbf{z}_n^{(i)} = \delta \phi_n^{\mathbf{Q}(i)} - \widetilde{\delta \phi_n^{\mathbf{Q}(i)}}$ as well as the ℓ_2 norm of the corresponding CG residual $\mathbf{r}_n^{(i)} := \mathbf{b}_n - \mathbf{A}_n \delta \phi_n^{\mathbf{Q}(i)}$ and the residual divided by the gap. This is demonstrated for the Sternheimer equation corresponding to the highest occupied eigenvalue $\epsilon_{N_{\text{occ}}}$, which is associated with the worst conditioning. For (A) the aluminium supercell the bound closely follows the ℓ_2 error but sometimes undershoots while for (B) the Heusler system the ℓ_2 error is even bounded by the residual norm — see Section 4 for more details on the setup of these numerical experiments.

Appendix D. Growth of Kernel-vector-product norm. In Section 3.3.2 of the main text we argue that given appropriate preconditioning of the GMRES, the Hartree-exchange-correlation kernel term $\|\mathbf{K} \mathbf{v}_i\|$ can be dropped from the prefactor

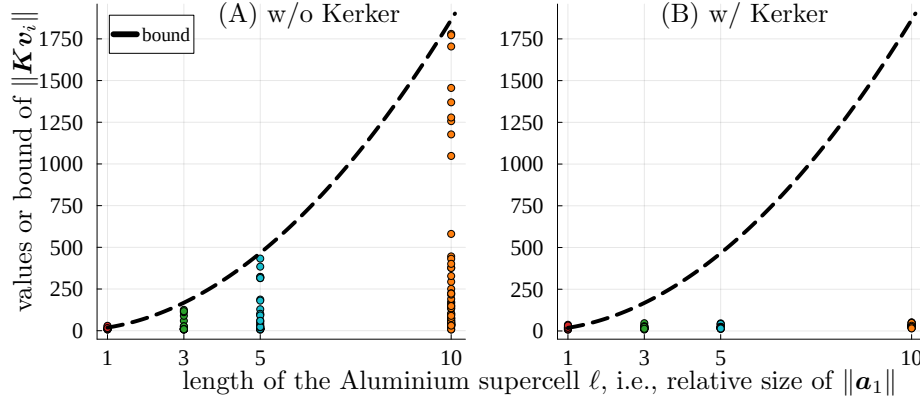


Fig. 6: Values of $\|Kv_i\|$ (circles) during the GMRES iterations for Aluminium supercell systems of different sizes (A) without and (B) with Kerker preconditioning. We employ the **agr** strategy to set the CG tolerances (see Table 1) and use ℓ to denote the factor by which \mathbf{a}_1 grows relative to the smallest Aluminium system, see Section 4.2 for details on the computational setup.

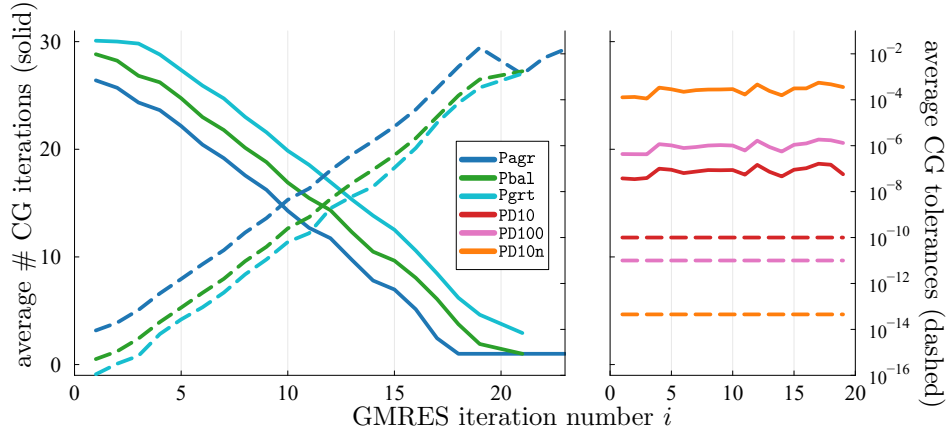


Fig. 7: Average number of CG iterations (in solid lines) and geometric average of CG tolerances (in dashed lines) per GMRES iteration of the aluminium supercell system discussed in Section 4.2.

$C_{i,n}$ of Theorem 3.7. Indeed, Figure 6 shows for the aluminium supercell, that the appropriate Kerker preconditioner enables to overcome the quadratic increase of this term with system size, i.e. that bound (3.15) is far too pessimistic.

Appendix E. Variation of CG iterations and tolerance across GMRES steps. Figure 7 shows how the CG tolerances employed for solving the Sternheimer equations evolve during the GMRES iterations. With respect to averaging over all (n, \mathbf{k}) we show both the average tolerance $\tau_{i,n\mathbf{k}}^{\text{CG}}$ as well as the average number of CG iterations per GMRES iteration i for the preconditioned strategies. Note that one Hamiltonian application is needed per CG iteration. For the baseline strategies (right hand side) the CG tolerances are fixed constants and thus the CG iterations remain almost constant across the GMRES iterations. In contrast, our adaptive strategies

(left hand side) require looser CG tolerances as the GMRES progresses and notably, initially employ tighter CG tolerances than the baselines, but near convergence only require 1 or 2 CG iterations for each SE. This behaviour suggests that the accuracy of the first few matrix-vector products effectively limits the final solution accuracy, which cannot be compensated by computing the matrix-vector product $\mathcal{E}\mathbf{v}$ more precisely in later GMRES iterations.

Appendix F. Testing size and GMRES parameter dependence. With respect to the aluminium system already considered in Section 4.2 we study the performance of the CG tolerance strategies from Table 1 as the system size, the Krylov subspace m and the targeted GMRES tolerance τ are varied. We keep the computational setup described in Section 4.2 and consider aluminium supercells in which the 4-atom cubic unit cell is repeated ℓ times along the x direction where $\ell = 1, 3, 5, 10$. For $\ell = 10$ we thus obtain exactly the system studied before. We use the same parameters as in Section 4.2 with the exception of the unit cell $\ell = 1$ where we set the \mathbf{k} -point grid to $3 \times 3 \times 3$. Additionally, on the extremely simple unit cell system ($\ell = 1$) we do not test **Pgrt** and **PD10n** strategies.

We test GMRES restart sizes of $m = 10$ and 20 , and do not consider smaller values. Note that even storing $m = 20$ Krylov vectors — amounting to $mN_g \approx 360N_b$ FP64 numbers — is a small memory cost compared to the amount of storage required for the occupied orbitals. The latter are complex-valued and thus require $2N_{\text{occ}}N_b \approx 1100N_b$ FP64 numbers for the largest system with $\ell = 10$. For the GMRES tolerance, we focus on $\tau = 10^{-6}$ and 10^{-9} , as other values are of limited relevance for practical applications. Our results are summarised in Tables 5, 6 and 7 with an even more comprehensive study available in the file `A1/data_logs/summary_tables.md` in our GitHub repository¹. Similar studies for the Heusler system are also available in the file `Fe2MnAl/data_logs/summary_tables.md` in the same repository. Throughout this study our adaptive strategies consistently outperform the baseline approaches with **Pbal** providing the best compromise between reliably achieving the desired tolerance τ and required number of Hamiltonian applications.

ℓ, m, τ	Pagr	Pbal	Pgrt	PD10	PD100	PD10n
1, 10, 10^{-9}	1.63	1.55		1.00	1.00	
3, 10, 10^{-9}	1.60	1.52	1.35	1.00	1.00	0.99
5, 10, 10^{-9}	1.47	1.51	1.35	1.00	0.99	0.98
10, 10, 10^{-9}	1.61	1.55	1.40	1.00	1.00	0.98
10, 20, 10^{-9}	1.53	1.47	1.32	1.00	0.99	0.98
10, 10, 10^{-6}	1.59	1.54	1.31	1.00	1.04	0.98
10, 20, 10^{-6}	1.43	1.39	1.26	1.00	1.04	0.99

Table 5: Relative efficiency η_{rel} (referencing PD10) for the aluminium systems with varied ℓ, m and τ . Our adaptive strategies are highlighted in blue, and the top three strategies for each metric are highlighted in orange.

¹https://github.com/bonans/inexact_Krylov_response

ℓ, m, τ	Pagr	Pbal	Pgrt	PD10	PD100	PD10n
1, 10, 10^{-9}	$1.37 \cdot 10^{-9}$	$2.96 \cdot 10^{-10}$		$1.43 \cdot 10^{-8}$	$1.19 \cdot 10^{-9}$	
3, 10, 10^{-9}	$1.08 \cdot 10^{-8}$	$7.73 \cdot 10^{-10}$	$3.27 \cdot 10^{-10}$	$2.46 \cdot 10^{-7}$	$2.06 \cdot 10^{-8}$	$6.92 \cdot 10^{-10}$
5, 10, 10^{-9}	$1.12 \cdot 10^{-8}$	$5.99 \cdot 10^{-10}$	$1.36 \cdot 10^{-10}$	$8.01 \cdot 10^{-7}$	$7.63 \cdot 10^{-8}$	$1.32 \cdot 10^{-9}$
10, 10, 10^{-9}	$4.34 \cdot 10^{-8}$	$1.50 \cdot 10^{-9}$	$1.94 \cdot 10^{-10}$	$8.69 \cdot 10^{-6}$	$6.96 \cdot 10^{-7}$	$3.16 \cdot 10^{-9}$
10, 20, 10^{-9}	$1.74 \cdot 10^{-8}$	$7.17 \cdot 10^{-10}$	$2.41 \cdot 10^{-10}$	$1.33 \cdot 10^{-5}$	$1.33 \cdot 10^{-6}$	$5.32 \cdot 10^{-9}$
10, 10, 10^{-6}	$7.03 \cdot 10^{-5}$	$1.12 \cdot 10^{-6}$	$2.41 \cdot 10^{-7}$	$8.54 \cdot 10^{-3}$	$7.44 \cdot 10^{-4}$	$4.12 \cdot 10^{-6}$
10, 20, 10^{-6}	$2.98 \cdot 10^{-5}$	$7.71 \cdot 10^{-7}$	$6.38 \cdot 10^{-8}$	$1.32 \cdot 10^{-2}$	$1.09 \cdot 10^{-3}$	$6.29 \cdot 10^{-6}$

Table 6: Accuracy of the returned solution $\|\mathbf{r}_{\text{end}}\|$ for the aluminium systems with varied ℓ, m and τ . Our adaptive strategies are highlighted in blue, and the top three strategies for each metric are highlighted in orange.

ℓ, m, τ	Pagr	Pbal	Pgrt	PD10	PD100	PD10n
1, 10, 10^{-9}	17 k	19 k		25 k	28 k	
3, 10, 10^{-9}	35 k	41 k	47 k	49 k	55 k	63 k
5, 10, 10^{-9}	80 k	86 k	101 k	97 k	109 k	130 k
10, 10, 10^{-9}	183 k	215 k	253 k	233 k	263 k	332 k
10, 20, 10^{-9}	168 k	196 k	228 k	194 k	219 k	275 k
10, 10, 10^{-6}	96 k	121 k	152 k	113 k	127 k	180 k
10, 20, 10^{-6}	101 k	124 k	152 k	99 k	113 k	159 k

Table 7: Total number of Hamiltonian applications N^{Ham} . Our adaptive strategies are highlighted in blue, and the top three strategies for each metric are highlighted in orange.

Acknowledgments. We would like to acknowledge fruitful discussions with Peter Benner, Gaspard Kemplin and Xiaobo Liu.

REFERENCES

- [1] S. L. ADLER, *Quantum theory of the dielectric constant in real solids*, Phys. Rev. (2), 126 (1962), pp. 413–420, <https://doi.org/10.1103/PhysRev.126.413>.
- [2] W. BAO AND Y. CAI, *Mathematical theory and numerical methods for Bose-Einstein condensation*, Kinet. Relat. Models, 6 (2013), pp. 1–135, <https://doi.org/10.3934/krm.2013.6.1>.
- [3] S. BARONI, S. DE GIRONCOLI, A. DAL CORSO, AND P. GIANNOZZI, *Phonons and related crystal properties from density-functional perturbation theory*, Rev. Mod. Phys., 73 (2001), pp. 515–562, <https://doi.org/10.1103/RevModPhys.73.515>.
- [4] S. BARONI, P. GIANNOZZI, AND A. TESTA, *Green’s-function approach to linear response in solids*, Phys. Rev. Lett., 58 (1987), pp. 1861–1864, <https://doi.org/10.1103/PhysRevLett.58.1861>.
- [5] J. BEZANSON, A. EDELMAN, S. KARPINSKI, AND V. B. SHAH, *Julia: a fresh approach to numerical computing*, SIAM Rev., 59 (2017), pp. 65–98, <https://doi.org/10.1137/141000671>.
- [6] E. CANCÈS, *Planewave DFT calculations*. DFTK School 2022, Aug. 2022, https://school2022.dftk.org/assets/Cances_PlaneWave_DFT.pdf (accessed 2025-04-17).
- [7] E. CANCÈS, R. CHAKIR, AND Y. MADAY, *Numerical analysis of nonlinear eigenvalue problems*, J. Sci. Comput., 45 (2010), pp. 90–117, <https://doi.org/10.1007/s10915-010-9358-1>.

- [8] E. CANCÈS, A. DELEURENCE, AND M. LEWIN, *A new approach to the modeling of local defects in crystals: the reduced Hartree-Fock case*, Comm. Math. Phys., 281 (2008), pp. 129–177, <https://doi.org/10.1007/s00220-008-0481-x>.
- [9] E. CANCÈS, V. EHRLACHER, D. GONTIER, A. LEVITT, AND D. LOMBARDI, *Numerical quadrature in the Brillouin zone for periodic Schrödinger operators*, Numer. Math., 144 (2020), pp. 479–526, <https://doi.org/10.1007/s00211-019-01096-w>.
- [10] E. CANCÈS, M. HASSAN, AND L. VIDAL, *Modified-operator method for the calculation of band diagrams of crystalline materials*, Math. Comp., 93 (2024), pp. 1203–1245, <https://doi.org/10.1090/mcom/3897>.
- [11] E. CANCÈS, M. F. HERBST, G. KEMLIN, A. LEVITT, AND B. STAMM, *Numerical stability and efficiency of response property calculations in density functional theory*, Lett. Math. Phys., 113 (2023), pp. Paper No. 21, 32, <https://doi.org/10.1007/s11005-023-01645-3>.
- [12] E. CANCÈS, G. KEMLIN, AND A. LEVITT, *Convergence analysis of direct minimization and self-consistent iterations*, SIAM J. Matrix Anal. Appl., 42 (2021), pp. 243–274, <https://doi.org/10.1137/20M1332864>.
- [13] E. CANCÈS, A. LEVITT, Y. MADAY, AND C. YANG, *Numerical Methods for Kohn–Sham Models: Discretization, Algorithms, and Error Analysis*, Springer International Publishing, Cham, 2023, pp. 333–400, <https://doi.org/10.1007/978-3-031-22340-2.7>.
- [14] E. CANCÈS AND M. LEWIN, *The dielectric permittivity of crystals in the reduced Hartree-Fock approximation*, Arch. Ration. Mech. Anal., 197 (2010), pp. 139–177, <https://doi.org/10.1007/s00205-009-0275-0>.
- [15] E. CANCÈS AND N. MOURAD, *A mathematical perspective on density functional perturbation theory*, Nonlinearity, 27 (2014), pp. 1999–2033, <https://doi.org/10.1088/0951-7715/27/9/1999>.
- [16] I. CATTO, C. LE BRIS, AND P.-L. LIONS, *The mathematical theory of thermodynamic limits: Thomas-Fermi type models*, Oxford Mathematical Monographs, Oxford University Press, 1998, <https://doi.org/10.1093/oso/9780198501619.001.0001>.
- [17] L. CHANUSSOT, A. DAS, S. GOYAL, T. LAVRIL, M. SHUAIBI, M. RIVIERE, K. TRAN, J. HERAS-DOMINGO, C. HO, W. HU, A. PALIZHATI, A. SRIRAM, B. WOOD, J. YOON, D. PARIKH, C. L. ZITNICK, AND Z. ULISSI, *Open catalyst 2020 (oc20) dataset and community challenges*, ACS Catalysis, 11 (2021), pp. 6059–6072, <https://doi.org/10.1021/acscatal.0c04525>.
- [18] Y. CHEN, L. ZHANG, H. WANG, AND W. E, *DeePKS: A comprehensive data-driven approach toward chemically accurate density functional theory*, J. Chem. Theory Comput., 17 (2021), pp. 170–181, <https://doi.org/10.1021/acs.jctc.0c00872>.
- [19] G. DUSSON AND Y. MADAY, *A posteriori analysis of a nonlinear Gross-Pitaevskii-type eigenvalue problem*, IMA J. Numer. Anal., 37 (2017), pp. 94–137, <https://doi.org/10.1093/imanum/drw001>.
- [20] H.-R. FANG AND Y. SAAD, *Two classes of multisection methods for nonlinear acceleration*, Numer. Linear Algebra Appl., 16 (2009), pp. 197–221, <https://doi.org/10.1002/nla.617>.
- [21] C.-R. GERHORST, A. NEUKIRCHEN, D. A. KLÜPPELBERG, G. BIHLMAYER, M. BETZINGER, G. MICHALICEK, D. WORTMANN, AND S. BLÜGEL, *Phonons from density-functional perturbation theory using the all-electron full-potential linearized augmented plane-wave method FLEUR*, Electron. Struct., 6 (2024), p. 017001, <https://doi.org/10.1088/2516-1075/ad1614>.
- [22] S. GOEDECKER, M. TETER, AND J. HUTTER, *Separable dual-space Gaussian pseudopotentials*, Phys. Rev. B, 54 (1996), pp. 1703–1710, <https://doi.org/10.1103/PhysRevB.54.1703>.
- [23] D. GONTIER AND S. LAHBABI, *Convergence rates of supercell calculations in the reduced Hartree-Fock model*, ESAIM Math. Model. Numer. Anal., 50 (2016), pp. 1403–1424, <https://doi.org/10.1051/m2an/2015084>.
- [24] X. GONZE, *Adiabatic density-functional perturbation theory*, Phys. Rev. A, 52 (1995), p. 1096, <https://doi.org/10.1103/PhysRevA.52.1096>.
- [25] X. GONZE, *Perturbation expansion of variational principles at arbitrary order*, Phys. Rev. A, 52 (1995), pp. 1086–1095, <https://doi.org/10.1103/physreva.52.1086>.
- [26] X. GONZE, *First-principles responses of solids to atomic displacements and homogeneous electric fields: Implementation of a conjugate-gradient algorithm*, Phys. Rev. B, 55 (1997), pp. 10337–10354, <https://doi.org/10.1103/physrevb.55.10337>.
- [27] X. GONZE, S. ROSTAMI, AND C. TANTARDINI, *Variational density functional perturbation theory for metals*, Phys. Rev. B, 109 (2024), <https://doi.org/10.1103/physrevb.109.014317>.
- [28] X. GONZE AND J.-P. VIGNERON, *Density-functional approach to nonlinear-response coefficients of solids*, Phys. Rev. B, 39 (1989), pp. 13120–13128, <https://doi.org/10.1103/PhysRevB.39.13120>.
- [29] C. HARTWIGSEN, S. GOEDECKER, AND J. HUTTER, *Relativistic separable dual-space gaussian*

- pseudopotentials from H to Rn* , Phys. Rev. B, 58 (1998), pp. 3641–3662, <https://doi.org/10.1103/PhysRevB.58.3641>.
- [30] M. F. HERBST AND A. LEVITT, *Black-box inhomogeneous preconditioning for self-consistent field iterations in density functional theory*, J. Phys. Condens. Matter, 33 (2020), p. 085503, <https://doi.org/10.1088/1361-648X/abcdbd>.
 - [31] M. F. HERBST AND A. LEVITT, *A robust and efficient line search for self-consistent field iterations*, J. Comput. Phys., 459 (2022), p. 111127, <https://doi.org/10.1016/j.jcp.2022.111127>.
 - [32] M. F. HERBST, A. LEVITT, AND E. CANCÈS, *A posteriori error estimation for the non-self-consistent kohn–sham equations*, Faraday Discuss., 224 (2020), pp. 227–246, <https://doi.org/10.1039/D0FD00048E>.
 - [33] M. F. HERBST, A. LEVITT, AND E. CANCÈS, *DFTK: A Julian approach for simulating electrons in solids*, Proc. JuliaCon Conf., 3 (2021), p. 69, <https://doi.org/10.21105/jcon.00069>.
 - [34] M. R. HESTENES AND E. STIEFEL, *Methods of conjugate gradients for solving linear systems*, J. Res. Natl. Bur. Stand., 49 (1952), pp. 409–436, <https://doi.org/10.6028/jres.049.044>.
 - [35] R. A. HORN AND C. R. JOHNSON, *Topics in matrix analysis*, Cambridge University Press, Cambridge, 1991, <https://doi.org/10.1017/CBO9780511840371>.
 - [36] M. F. KASIM AND S. M. VINKO, *Learning the exchange-correlation functional from nature with fully differentiable density functional theory*, Phys. Rev. Lett., 127 (2021), <https://doi.org/10.1103/physrevlett.127.126403>.
 - [37] G. P. KERKER, *Efficient iteration scheme for self-consistent pseudopotential calculations*, Phys. Rev. B, 23 (1981), pp. 3082–3084, <https://doi.org/10.1103/PhysRevB.23.3082>.
 - [38] S. KIRKLIN, J. E. SAAL, B. MEREDIG, A. THOMPSON, J. W. DOAK, M. AYKOL, S. RÜHL, AND C. WOLVERTON, *The open quantum materials database (OQMD): assessing the accuracy of DFT formation energies*, npj Comput. Mater., 1, 15010 (2015), <https://doi.org/10.1038/npjcompumats.2015.10>.
 - [39] J. KIRKPATRICK, B. MCMORROW, D. H. P. TURBAN, A. L. GAUNT, J. S. SPENCER, A. G. D. G. MATTHEWS, A. OBIKA, L. THIRY, M. FORTUNATO, D. PFAU, L. R. CASTELLANOS, S. PETERSEN, A. W. R. NELSON, P. KOHLI, P. MORI-SÁNCHEZ, D. HASSABIS, AND A. J. COHEN, *Pushing the frontiers of density functionals by solving the fractional electron problem*, Science, 374 (2021), pp. 1385–1389, <https://doi.org/10.1126/science.abj6511>.
 - [40] A. D. LEWIS, *A top nine list: Most popular induced matrix norms*, 2023, <https://arxiv.org/abs/2309.07190>.
 - [41] L. LIN AND J. LU, *A mathematical introduction to electronic structure theory*, SIAM, Philadelphia, PA, 2019, <https://doi.org/10.1137/1.9781611975802>.
 - [42] L. LIN, J. LU, AND L. YING, *Numerical methods for Kohn–Sham density functional theory*, Acta Numer., 28 (2019), pp. 405–539, <https://doi.org/10.1017/s0962492919000047>.
 - [43] L. LIN, Z. XU, AND L. YING, *Adaptively compressed polarizability operator for accelerating large scale ab initio phonon calculations*, Multiscale Model. Simul., 15 (2017), pp. 29–55, <https://doi.org/10.1137/16M1077325>.
 - [44] H. J. MONKHORST AND J. D. PACK, *Special points for Brillouin-zone integrations*, Phys. Rev. B, 13 (1976), pp. 5188–5192, <https://doi.org/10.1103/PhysRevB.13.5188>.
 - [45] P. NORMAN, K. RUUD, AND T. SAUE, *Principles and Practices of Molecular Properties: Theory, Modeling and Simulations*, John Wiley & Sons, Ltd, Chichester, UK, 2018, <https://doi.org/10.1002/9781118794821>.
 - [46] J. P. PERDEW, K. BURKE, AND M. ERNZERHOF, *Generalized gradient approximation made simple*, Phys. Rev. Lett., 77 (1996), pp. 3865–3868, <https://doi.org/10.1103/PhysRevLett.77.3865>.
 - [47] M. REED AND B. SIMON, *Methods of modern mathematical physics. IV. Analysis of operators*, Academic Press, 1978, <https://doi.org/10.1016/B978-0-12-585001-8.X5001-6>.
 - [48] N. RIVANO, N. MARZARI, AND T. SOHIER, *Density functional perturbation theory for one-dimensional systems: Implementation and relevance for phonons and electron-phonon interactions*, Phys. Rev. B, 109 (2024), p. 245426.
 - [49] Y. SAAD AND M. H. SCHULTZ, *GMRES: a generalized minimal residual algorithm for solving nonsymmetric linear systems*, SIAM J. Sci. Statist. Comput., 7 (1986), pp. 856–869, <https://doi.org/10.1137/0907058>.
 - [50] V. SIMONCINI AND D. B. SZYLD, *Theory of inexact Krylov subspace methods and applications to scientific computing*, SIAM J. Sci. Comput., 25 (2003), pp. 454–477, <https://doi.org/10.1137/S1064827502406415>.
 - [51] M. P. TETER, M. C. PAYNE, AND D. C. ALLAN, *Solution of Schrödinger’s equation for large systems*, Phys. Rev. B, 40 (1989), pp. 12255–12263, <https://doi.org/10.1103/PhysRevB.40.12255>.
 - [52] J. VAN DEN ESHOF AND G. L. G. SLEIJPEN, *Inexact Krylov subspace methods for linear sys-*

- tems*, SIAM J. Matrix Anal. Appl., 26 (2004), pp. 125–153, <https://doi.org/10.1137/S0895479802403459>.
- [53] H. F. WALKER AND P. NI, *Anderson acceleration for fixed-point iterations*, SIAM J. Numer. Anal., 49 (2011), pp. 1715–1735, <https://doi.org/10.1137/10078356X>.
 - [54] W. WINDL, P. PAVONE, K. KARCH, O. SCHÜTT, D. STRAUCH, P. GIANNOZZI, AND S. BARONI, *Second-order raman spectra of diamond from ab initio phonon calculations*, Phys. Rev. B, 48 (1993), pp. 3164–3170, <https://doi.org/10.1103/PhysRevB.48.3164>.
 - [55] J. WU, S.-M. PUN, X. ZHENG, AND G. CHEN, *Construct exchange-correlation functional via machine learning*, J. Chem. Phys., 159 (2023), <https://doi.org/10.1063/5.0150587>.